Light trapping in thin silicon waveguides by plasmon mediated mode coupling

Jorik van de Groep

Supervisors:
Pierpaolo Spinelli MSc., Claire van Lare MSc. and Prof. Dr. Albert Polman

Abstract

Thin-film solar cells have many advantages over their thick counterparts. However, these cells often exhibit relatively poor light absorption. Efficient light trapping by coupling light into the discrete set of waveguide modes supported by such thin semiconductor films, enhances the absorption significantly. Here, two-dimensional metal nanoparticle arrays on top of a SOI wafer are studied, to investigate the mode coupling mechanism. The 200 nm top Si layer of the SOI wafer acts as an isolated waveguide that functions as a model system for a thin-film solar cell.

Analytical calculations and finite-element simulations are used to find the waveguide modes supported by the structure, to determine their dispersion and calculate the absorption enhancement inside the waveguide due to mode coupling. Based on these calculations we describe the coupling mechanism in terms of mode overlap and momentum matching between the incoming light and the waveguide modes. Using a novel soft imprint technique, two-dimensional particle arrays with different particle diameter and pitch are fabricated on top of SOI wafers to experimentally study the mode coupling mechanism. Spectrally resolved total reflection measurements and angle-resolved specular reflection measurements are used to detect light coupling to waveguide modes.

A new method to directly probe the insitensity enhancement inside semiconductor layers is presented in which optically active erbium ions that luminesce in the IR are implanted in the waveguide. The PL intensity is used as a measure of the erbium excitation rate. This method is then used to prove that light couples to waveguide modes. By changing the angle of incidence of the pump light, clear distinct peaks are observed for different angles as a result of momentum matching, that are attributed to coupling to well-defined waveguide modes.

Motivated by this work, a two-dimensional network of silver nanowires is designed and fabricated to replace ITO as a transparent conducting electrode on optoelectronic devices. By changing the wire dimensions, the resonant behaviour of the wires can be tuned to optimize the transmittance. Transmission measurements and electrical I-V measurements show supernormal optical transmittance, which is higher than for commercially used ITO over the $400 - 600$ nm spectral range. Also, the electrical resistance of the networks has the potential to beat the ITO when scaled to large areas.

Contents

Chapter 1

Introduction

1.1 Introduction

In the search for new and sustainable energy sources, solar energy plays an important role. The global contribution of electricity generated by photovoltaics (PV) is expected to increase from 0.1% up to 11% before 2050 [1]. However, the current costs of such electricity are still a factor 2-5 too high in order to efficiently compete with fossil energy sources. Important methods to lower the costs is achieving higher conversion efficiencies and reducing material costs. In second generation solar cells, the cell thickness is reduced in order to suppress the material costs. These so called thin-film cells are cheap, but exhibit poor light absorption and thereby low efficiencies. To improve the performance of solar cells, it is necessary to understand the loss mechanisms. The thermodynamics of the loss processes and the theoretical upper efficiency limit of wafer based silicon solar cells have been studied extensively and are well understood [2–7]. Based on this work, new concept designs aiming for extremely high efficiencies have been introduced, called third generation solar cells. These include amongst others multi-junction cells [8, 9], hot carrier cells [8, 10], quantum dot cells [11] and nanowire based cells [12]. However, due to their complex designs many fundamental and technological challenges need to be overcome in order to obtain commercial products. A separate branch of third generation PV is focusing on enhancing the performance and reducing the costs of second generation thin-film solar cells that already are commercially available. Cost reduction is achieved by reducing the cell thickness further down to below the wavelength of light. Besides cost reduction, thinner cells have other advantages for PV applications such as: suitability for small minority carrier diffusion lengths [13]; higher open circuit voltages due to reduced bulk recombination [13]; and for amorphous silicon cells a smaller reduction in cell efficiency due to the reduced Stabler-Wronski effect [14]. However, ultra-thin cells absorb an even smaller fraction of the incoming light. Advanced light trapping schemes are therefore needed to force as much light as possible to be absorbed in the active layer.

Light trapping was first explored by Yablonovitch who, using a statistical ray optics model, derived the maximum absorption enhancement in thick wafers as a result of random on texturing the interface and using a back reflector [15, 16]. This upper limit for the absorption enhancement with respect to the single pass absorption is $4n^2$ for wavelengths close to the bandgap, where n is the refractive index of the slab. This model is based on total angular randomization of the wave vectors of the light-rays - like scattering from a Lambertian surface - within several internal reflections. Since this only occurs in ergodic media, this limit is often referred to as the ergodic limit. In view of the necessity of light trapping for thin-film solar cells, a lot of work has been performed both on the fundamental knowledge on light trapping [17] as well as modeling [18, 19] and experimental applications [13, 20]. Random texturing becomes impossible when the layer thickness reduces below the average feature size. Therefore this design cannot be used for ultra thin cells unless the cell is grown on top of the rough surface conformally. On the other hand, thin film solar cells support a discrete and limited set of guided mode in the high refractive index active layer. Coupling light into these waveguide modes proves to be a very efficient method of light trapping, able to enhance the absorption significantly.

More recently, it is recognized that the use of plasmonic metal nanoparticles can be very beneficial for PV applications. Due to the collective oscillations of the free electrons driven by the electric component of incoming light, metal nanoparticles exhibit strong resonances characterized by high scattering cross

sections. Several design concepts have been proposed to exploit this resonant behavior in order to enhance solar cell performance [21]: particles inside the active layer acting as resonant antennas, corrugated metal back reflectors scattering light into waveguide modes, and particles on top to scatter light efficiently into the solar cell. Corrugated back reflectors have already been realized experimentally and have shown significant efficiency increases that can be attributed to light coupling to waveguide modes [13, 22, 23]. However, this method requires conformal growth of a-Si solar cells on top of nanopatterned and prefabricated back reflectors. Particles on top of solar cells have many potential applications since they are easily applicable on consisting cell designs and can easily be introduced in standard production processes. Metal nanoparticles on top of solar cells are beneficial for two reasons. First, metal nanoparticles radiate as oscillating dipoles after excitation. Calculations have shown that dipoles close to the interface of a high index material preferentially scatter light into the substrate as a result of the higher local density of states [24]. This principle can be used for optical impedance matching. Spinelli *et al.* have shown that a combination of silver nanoparticle arrays in combination with a Si_3N_4 anti-reflection coating provide better incoupling of light than commercially used Si_3N_4 layers [25]. Second, light that is scattered by the particles is scattered with an angular distribution [24]. This directly results in a path length enhancement for the light inside the cell [21]. Furthermore, if the scattered angle is large enough, light can couple to waveguide modes supported by the cell. Several systematic studies have investigated the influence of particle shape, size, dielectric environment [26, 27], different metals and use of spacer layers [24], and the scattering of light into photonic waveguide modes. Also the coupling to surface plasmon polariton modes has been studied [27, 28].

Positioning two dimensional arrays of metal nanoparticles on top of optically active layers causes coupling between particles and the active layer. The inter particle coupling is strongly influenced by the presence of modes in the active layer as was first recognized by Stuart&Hall [29], who also realized that metal nanoparticles can enhance the sensitivity of photodetectors [30, 31]. The collective scattering of periodic arrays can also function as a two dimensional grating and therefore generate in plane momentum [32]. This allows light to couple to waveguide modes with high in-plane wave vectors and thereby enhance the optical path-length through light trapping. Gratings have been recognized as efficient couplers for waveguides before [33, 34], but combining plasmonic particle arrays with thin film solar cells gives rise to different physics than dielectric one-dimensional gratings. The interaction between plasmon resonances localized on single particles and the diffraction from the collective array [35] and the lattice surface modes as a result of this interaction [36–38] are examples of complicated mechanisms playing a role.

In this work we investigate the interaction between large two-dimensional metal nanoparticle arrays on top of thin-film solar cells and the waveguide modes supported by this high-index thin film. We use a novel inexpensive soft-imprint method [39, 40], to fabricate metal particle arrays as large as 4×4 mm, enabling for the first time to experimentally investigate this interaction in large detail. The angular redistribution and diffractive scattering as a result of these arrays provide the in-plane momentum to couple to waveguide modes. Since coupling to waveguide modes is one of the most effective mechanisms of light trapping, understanding the coupling mechanism is important for thin-film solar cells. However, as mentioned above, the physics of plasmonic particle arrays on top of a waveguide is very complex. Moreover, investigating the coupling to waveguide modes by probing the photocurrent generated by an actual solar cell also requires taking all the electrical characteristics of the cell into account. To decouple the effect of light incoupling and electrical carrier collection, we introduce a new method to directly probe the light field intensity inside the semi-conductor layer. We use a Silicon-On-Insulator (SOI) wafer - where the top silicon layer serves as a model system for a thin-film solar cell. The Si layer is doped with optically active erbium ions that are excited by waveguide modes at 980 nm. The fluorescence at 1.54 μm is used as a measure of the Er excitation rate. In this way the intensity enhancement in the Si layer can be directly probed [41]. We use analytical calculations, finite-element simulations, spectrally resolved total reflection measurements, angle-resolved specular reflection measurements and angle-resolved photoluminescence (PL) measurements to study the light trapping due to metal particle arrays with different particle diameter and pitch. We find clear peaks in the PL enhancement that are assigned to well-defined waveguide modes.

1.2   Outline

The remainder of this thesis is constructed as follows. In chapter 2, the theory of waveguide modes is presented and used to calculate the waveguide modes that are supported by the SOI wafer. The dispersion curves and thereby the in-plane momentum needed to couple to the waveguide modes are also calculated. Next, in chapter 3, finite-element simulations are used to investigate the optical reflection spectra that are obtained from patterned SOI wafers. We systematically investigate the influence of Fabry-Perot resonances, inter-particle coupling and plasmonic resonances on the reflection spectra. The simulations are also used to characterize the modes and to calculate the absorption enhancement as a result of coupling to waveguide modes. Chapter 4 discusses the fabrication of particle arrays and optical reflection measurements on different array designs. We compare simulations and calculations with the experimental spectra and identify the coupling to waveguide modes. In chapter 5 we present our new method in which the coupling to waveguide modes is directly detected with erbium as an optical probe. Finally, in chapter 6, we present a metal nanostructure that serves both to effectively couple light into the underlying substrate and conduct electrical current laterally over the surface. These transparent conducting networks, consisting of silver nanowires, may replace the indium-tin-oxide (ITO) layer used in a-Si and polymer solar cells. Final conclusions will be drawn in chapter 7.

Chapter 2

Waveguide modes in SOI wafers

2.1 Introduction

In order to understand light coupling to waveguide modes, as well as using it as a mechanism for light trapping, it is important to understand the basics of waveguide theory. To obtain this basic knowledge, the theory of waveguide modes is shortly discussed and then applied to the system that is used in experiments. The goal of these calculations is to learn about the characteristics of waveguide modes such as in-plane wave vectors, losses, mode profiles and dispersion curves, as well as how to couple to these waveguide modes. Furthermore, knowing which modes are supported by the substrates used in the experiments and their dispersion curves, allows us to compare the experimental results with the theoretical calculations.

Waveguide modes allow light to be trapped inside a layer of a high refractive index material. The most common waveguide is the optical fibre, where the core of the fibre has a slightly higher refractive index than the cladding. This allows light to be trapped in two dimensions, forcing propagation in the third. Calculating the modes supported by such a fibre is well understood [42, 43]. However, ultra thin-film solar cells resemble a slab waveguide, where confinement is limited to one dimension. The slab is assumed to be infinitely long in the other two dimensions. Although the size of a solar cells is limited, these lateral dimensions are almost infinite compared to the 200 nm thickness of for example an ultra thin-film solar cell. Thick slab waveguides can be described by ray optics, but for thicknesses in the order of the wavelength the solution of Maxwell's equations leads to discrete modes, i.e. electric field profiles across the waveguide thickness with a fixed wave vector k at a given frequency ω [32, 43]. In this work, we use the *transfer matrix method* using a formalism developed by Verhagen [44] to determine the waveguide modes including Surface Plasmon Polariton (SPP) modes supported by any arbitrary multi-layer structure, given the complex dielectric constant $\varepsilon = \varepsilon' + i\varepsilon''$ for all layers.

2.2 Theory

Assuming flat and infinite layers, any multilayer waveguide can be schematically described as in Fig. 2.1. Shown here is a stack of n layers. Layer j has a thickness d_j, a complex dielectric constant ε_j and the bottom of the layer is positioned at y_j. The structure has translational symmetry in x-z-plane, and the outer layers are assumed to be semi-infinite ($y_1 = -\infty$, $y_{n+1} = \infty$). To determine the eigenmodes supported by this structure, the wave equation needs to be solved in each layer assuming no waves incident from the outer layers. This can be done by using the transfer matrix method as described in ref. [44]. This method expresses all boundary conditions at all interfaces and the propagation of the fields throughout the layers in matrices. Eigenmodes exist when there is a solution for k_z that fulfills the dispersion relation:

$$Q_{n,11} - ik_{y1}Q_{n,12} + \frac{i}{k_{yn}}Q_{n,21} + \frac{k_{y1}}{k_{yn}}Q_{n,22} = 0 \tag{2.1}$$

Here $k_{yj} = \sqrt{\varepsilon_j k_0^2 - k_z^2}$ is the wave vector of the field in layer j in the y-direction. Furthermore,

$$Q_j = T_j \cdot M_{j-1} \cdot M_{j-2} \ldots M_2 \tag{2.2}$$

where T represents the boundary conditions between layer j and layer $j - 1$, and M_j represents the propagation of the field throughout layer j. Note that the definition of both T and M_j is different for
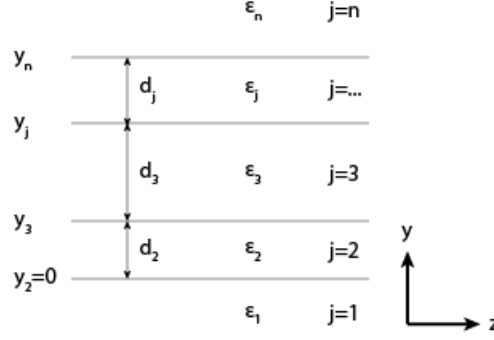
Figure 2.1: *Schematic of a n-layer structure with the layer number j, dielectric constant ε_j, lower limit y_j, and thickness d_j for each layer.*

TE and TM modes:

$$T_j^{TE} = \begin{pmatrix} 1 & 0 \\ 0 & 1 \end{pmatrix} \qquad\qquad T_j^{TM} = \begin{pmatrix} 1 & 0 \\ 0 & \frac{\varepsilon_j}{\varepsilon_{j-1}} \end{pmatrix} \qquad (2.3)$$

$$M_j^{TE} = \begin{pmatrix} cos(k_{yj}d_j) & \frac{1}{k_{yj}}sin(k_{yj}d_j) \\ -k_{yj}sin(k_{yj}d_j) & cos(k_{yj}d_j) \end{pmatrix} \qquad M_j^{TM} = \begin{pmatrix} cos(k_{yj}d_j) & \frac{\varepsilon_j}{k_{yj}\varepsilon_{j-1}}sin(k_{yj}d_j) \\ -k_{yj}sin(k_{yj}d_j) & \frac{\varepsilon_j}{\varepsilon_{j-1}}cos(k_{yj}d_j) \end{pmatrix}$$
$$(2.4)$$

From now on we will focus on TE polarization. From the solution of Eq. 2.1, the electric field distribution throughout the layers can be calculated:

$$E_j(z,y,t) = e^{i(k_z z - \omega t)}$$
$$\begin{pmatrix} E_0 e^{-ik_{y1}y} & j=1 \\ (Q_{j,11} - ik_{y1}Q_{j,12})E_0 cos(k_{yj}(y-y_j)) + (Q_{j,21} - ik_{y1}Q_{j,22})\frac{E_0}{k_{yj}}sin(k_{yj}(y-y_j)) & 2 \leq j \leq (n-1) \\ (Q_{n,11} - ik_{y1}Q_{n,12})E_0 e^{ik_{yn}(y-y_n)} & j=n \end{pmatrix} \hat{x}$$
$$(2.5)$$

The magnetic field components can be calculated from Eq. 2.5 by applying Faraday's law.

2.3 Modes supported by SOI wafer

The theoretical formalism described in section 2.2 can be used to determine the eigenmodes supported by a SOI wafer. The Nelder-Mead algorithm [45] is used to numerically solve Eq. 2.1 and find the in-plane wave vectors of the different modes. The geometry used in the calculations is the same as the layer structure of the SOI wafers that are used in the experiments. This layer structure, along with the definition of the axes, is shown in the inset of Fig. 2.2a. The SOI wafer consists out of a Si substrate, a 1 μm SiO$_2$ layer, and a 200 nm Si waveguide on top. The oxide layer isolates the Si waveguide on top from the substrate to prevent leakage in the substrate. In the calculations, the layers are assumed to be flat and infinite in the x and z dimension. Furthermore, the substrate is assumed to be semi-infinite. In some cases a top spacer layer consisting out of SiO$_2$ is used as well. Optical constants for Si are obtained from [46] and for SiO$_2$ from [47]. When solving Eq. 2.1 for this structure, the complex wave vector $k_z = \beta + i\kappa$ of the modes can be obtained. Using this wave vector, Eq. 2.5 can be used to obtain the field profiles. For TE-polarization this gives rise to definitions for $E_x(y)$, whereas for TM-polarization this gives the field profiles for $H_x(y)$. Assuming TE-polarization, the electric field profiles for this multilayer waveguide

are given by

$$E_j(z,y,t) = e^{i(k_z z - \omega t)}$$

$$\begin{pmatrix} E_0 e^{-ik_{y1}y} & j=1 & (S_iO_2) \\ (Q_{2,11} - ik_{y1}Q_{2,12})E_0 cos(k_{y2}(y-y_2)) + (Q_{2,21} - ik_{y1}Q_{2,22})\frac{E_0}{k_{y2}}sin(k_{y2}(y-y_2)) & j=2 & (S_i) \\ (Q_{3,11} - ik_{y1}Q_{3,12})E_0 cos(k_{y3}(y-y_3)) + (Q_{3,21} - ik_{y1}Q_{3,22})\frac{E_0}{k_{y3}}sin(k_{y3}(y-y_3)) & j=3 & (S_iO_2) \\ (Q_{n,11} - ik_{y1}Q_{n,12})E_0 e^{ik_{y4}(y-y_4)} & j=4 & (Air) \end{pmatrix} \hat{x}$$

$$(2.6)$$

with

$$Q_2 = \mathbb{1} \tag{2.7}$$

$$Q_3 = M_2 \tag{2.8}$$

$$Q_n = M_3 \cdot M_2 \tag{2.9}$$

For the 200 nm Si layer, five TE modes are found at a free-space wavelength of $\lambda_0 = 400$ nm ($k_0 = 15.71$ μm^{-1}). Figure 2.2b shows the electric field distribution for these modes. In the graphs, the vertical dashed lines indicate the interfaces between: the oxide layer and the waveguide, the waveguide and the spacer layer, and the spacer layer and air. The five different modes are all mainly localized in the Si waveguide. The in-plane wave vector k_z of each modes is indicated at the top of each graph and ranges from $\beta = 54.5$ to 86.8 μm^{-1} and $\kappa = 4.5$ to 6.4 μm^{-1}. Figure 2.2b shows that higher order modes are characterized by lower wave vectors (β) but with higher losses (κ). The latter is the result of the fact that for higher order modes, the evanescent tail of the mode profiles extends further in the non-absorbing oxide layers. Similar mode profiles can be obtained for the magnetic field in case of TM polarization. These are not shown here.

In Fig. 2.2a, the dispersion curve for all TE (red) and TM (blue) modes is shown for $0.4 < \lambda_0 < 1.5\mu m$. This figure shows how the in-plane wave vector β (horizontal axis) changes as a function of free space wave vector k_0 (vertical axis). The black dashed line corresponds to the light line in air. The horizontal error bars represent the uncertainty in β corresponding to the imaginary component of the wave vector κ, and thus to the absorption of the modes. This will be discussed in section 2.4. First of all, Fig. 2.2a shows that all modes are highly dispersive, especially at high values for k_0. This is a direct result of the highly dispersive nature of the Si waveguide. Second, all the dispersion curves are located below the light line. This indicates that the modes are purely bound and cannot couple to far field radiation. The fact that the dispersion curves end when the light line is approached is a direct result of the theoretical derivation, where we search solutions for purely bound modes only. The higher order modes do cross the light line for decreasing k_0 and can couple to far field radiation ('leaky modes'). Cut-off will occur for these modes when the dispersion curve crosses $\beta = 0$. Third, the TM modes are characterized by a slightly lower β than the corresponding TE modes. The dispersion curve of each mode indicates the amount of in-plane momentum that is needed to couple to this specific mode. Section 2.6 will discuss the implications of this in-plane momentum on the ability to couple to the waveguide modes using plasmonic scatterers.

2.4   Uncertainty in k_z

The imaginary component of k_z represents the propagation losses of a mode. Light trapped inside the waveguide mode propagates in the x-z-plane with a wavelength determined by β. However, when the waveguide consists of an absorbing material the intensity experiences a ring-down and the field can be described by a decaying cosine, as shown in Fig 2.3a. This results in an uncertainty in β. This uncertainty is calculated by taking the Fourier transform $F(k)$ of a decaying cosine and using $k_z = \beta + i\kappa$ of the waveguide mode to determine the spectral full-width at half-maximum (FWHM) for each k_0. An example of $F(k)$ is shown in Fig. 2.3b where the definition for $F(k)$ is also shown. The larger the absorption, the larger the uncertainty in k_z. The error bars in Fig. 2.2a correspond to the FWHM of the k spectra as in Fig. 2.3b, for each k_0. As can be seen in Fig. 2.2a, the uncertainty in β is larger at higher k_0: these values for k_0 correspond to wavelengths close to the direct bandgap of Si where the absorption is stronger. To study this effect in more detail, Fig. 2.3c shows the uncertainty in β for the TE0 mode for the SOI wafer as described in Fig. 2.2a (red), plotted for a more extended range to include the direct
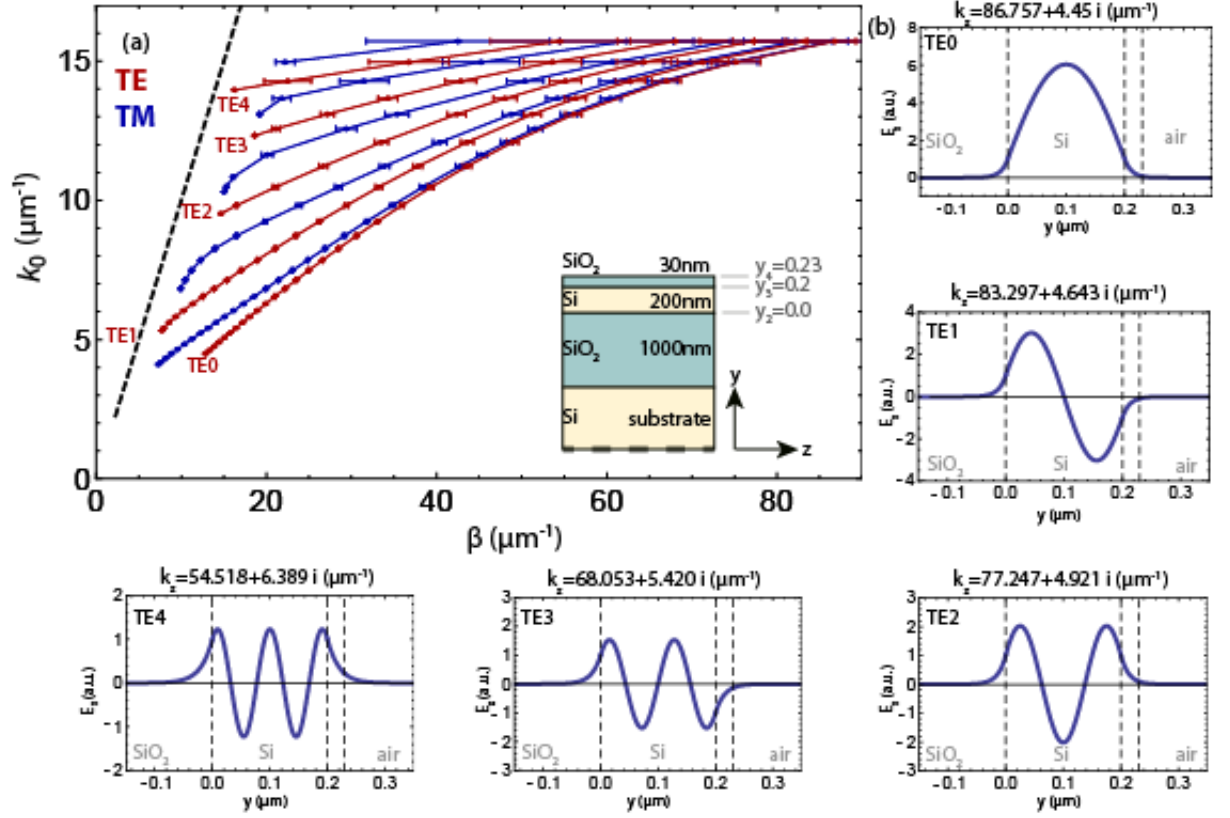
Figure 2.2: *a) The dispersion curve for the modes supported by the structure for $400nm\leq \lambda_0 \leq 1500nm$. Red corresponds to TE modes, blue to TM modes. The dashed black line represents the light line in air. The inset is a schematic of the multilayer waveguide consisting of a SOI wafer with a SiO_2 spacer layer on top. The top silicon layer acts as a waveguide. The layer is assumed to be infinite in the two in-plane directions. b) The five different TE modes supported by the waveguide $\lambda_0 = 400$ nm. The complex parallel wave vector is also given for each mode. The vertical dashed lines depicted are the interfaces between the different layers.*

bandgap of c-Si at short wavelengths. Also shown in Fig. 2.3c is the calculated dispersion curve for the TE0 mode inside an 145 nm thick a-Si layer (blue) of an ultra-thin film a-Si solar cell based on ref. [13]. The stronger absorption in a-Si gives a large broadening of the dispersion curve over a large range of k_0. At $k_0 \sim 18\mu m^{-1}$ the light is absorbed within the first cycle of the oscillation, with the result that k_z is no longer sharply defined. This becomes even more clear from the inset in Fig. 2.3c, which shows the propagation length of the TE0 mode, defined as $L_p = \frac{1}{2\kappa}$, for a-Si (blue) and c-Si (red). For c-Si, the absorption length is very small at high values for k_0, but increases by several orders of magnitude for lower k_0. The absorption length for the TE0 mode in the a-Si cell shows that the mode decays within $\sim 10^{-2}$ μm at high k_0.

2.5 Influence of spacer layer

In this work we will perform experiments on samples with and without a 30 nm thick SiO_2 spacer layer at the surface. The spacer layer was included in the calculations in section 2.3. To investigate the effect of the spacer layer on the dispersion, Fig. 2.4 shows the mode profiles and wave vectors of the TE0 mode for $\lambda_0 = 400$ nm (a) and $\lambda_0 = 1500$ nm (b). The blue line represents the mode profile for the layer structure with spacer layer and the red line the one without the spacer layer. In both cases the difference between the data with and without spacer layer is very small. At short wavelengths (Fig. 2.4a) the mode overlaps nearly fully with the Si waveguide layer and the evanescent tail sticking out of the waveguide - into the air or spacer layer - is small. The result is that the mode profile is not significantly altered by the presence of the spacer layer and the red line fully overlaps the blue. This is also reflected in the wave
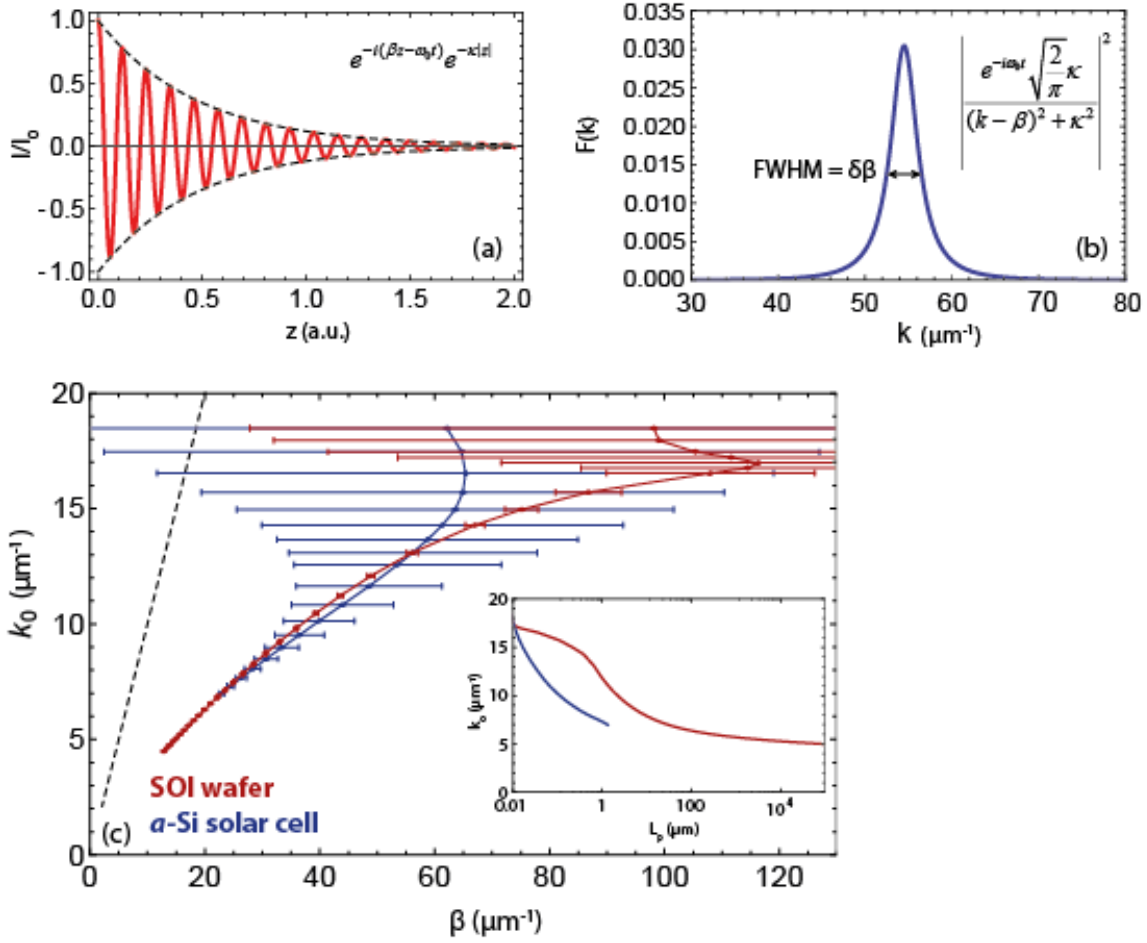
Figure 2.3: *a) An example of the ringdown of the field of a waveguide mode in an absorbing material, where the field can be described as a decaying cosine. **b)** Spectral image of the Fourier Transform of a decaying cosine, where the FWHM describes the uncertainty in β. **c)** The dispersion graph of the TE0 mode for the SOI wafer (red) as shown in Fig. 2.2c and the TE0 mode for an a-Si thin film solar cell (blue) with the layer thicknesses as in ref. [13]. This figure indicates how the stronger absorption in a-Si with respect to the c-Si waveguide in the SOI wafer results in more uncertainty in β. The absorption length of the modes is shown as an inset, showing that the mode inside the a-Si decays within one micrometer whereas in the c-Si waveguide it decays over several orders of magnitude larger distances at low k_0.*

vectors which are almost equal and also shown. At longer wavelengths (Fig. 2.4b), the mode does not completely fit into the waveguide and a larger evanescent tail is sticking into the spacer layer. However, the fraction of the mode overlapping the spacer layer is very small, so that the influence of the spacer layer is negligible. We conclude that the dispersion curves as shown in Fig. 2.2a can be used to compare with the measurements on the samples with and without a spacer layer.

2.6 Coupling to waveguide modes: momentum matching and mode overlap

As mentioned in section 2.3, the dispersion curve in Fig. 2.2a indicates the in-plane momentum corresponding to each mode. From Snell's law it can easily be derived that the in-plane component of the wave vector is conserved when a ray of light enters a medium. For this reason, light incident at normal incidence to the SOI waveguide structure, which has no in-plane wave vector component can not couple to a waveguide mode. Increasing the incident angle, momentum can be generated up to a value indicated by the light line. Depending on the angle of incidence θ with respect to the surface normal, the in-plane component of the wave vector of the incoming light varies between 0 and k_0: $0 \leq k_0 sin(\theta) \leq k_0$. This
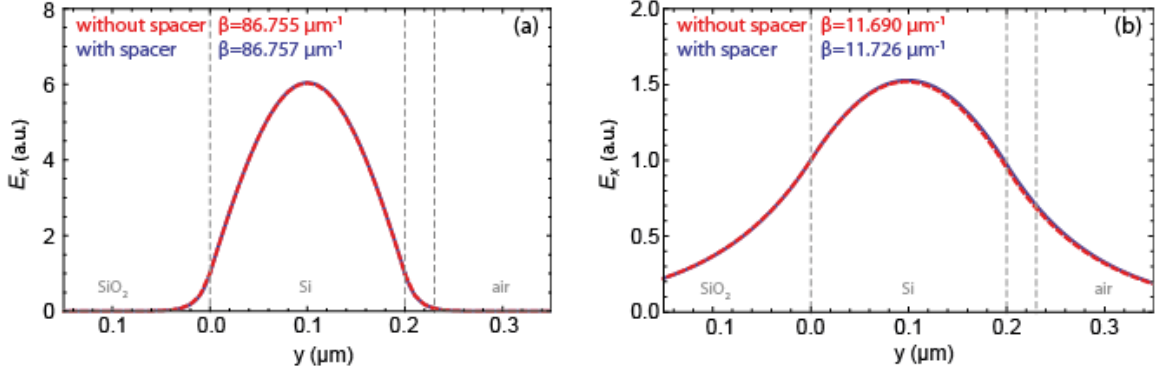
Figure 2.4: *The mode profile of the TE0 mode for **a)** $\lambda_0 = 400$ nm and **b)** $\lambda_0 = 1500$ nm in a structure with (blue) and without (red) a 30 nm SiO_2 spacer layer. The mode profiles almost fully overlap and the in-plane wave vector is nearly equal. The difference is larger for longer wavelengths because a larger fraction of the field is in the spacer layer due to the more slowly decaying evanescent field.*

means that the incoming light has a *mismatch* in terms of momentum with respect to the waveguide modes. This momentum mismatch has to be corrected for to couple light to any of the modes. In this work this is done by using a particle array as a two dimensional grating, as shown as inf Fig. 2.5a. The
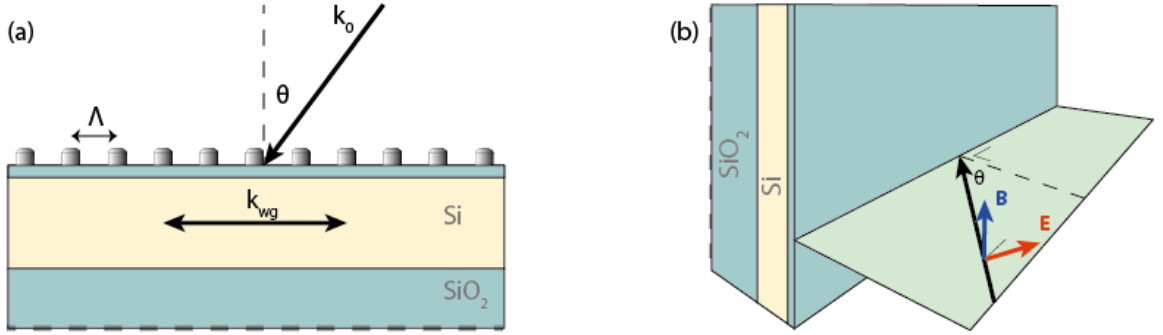

Figure 2.5: *a) Sketch of momentum matching needed to couple to waveguide modes. b) Mode overlap for p-polarized light coming in under an angle of incidence θ. Perfect mode overlap with the TM modes for the parallel $\vec{B}$ component. The mode overlap of the in-plane component of $\vec{E}$ with the TE modes is determined by θ.*

collective scattering from the particle array will result into different diffraction orders q that each scatter under a different angle. The in-plane momentum generated by a grating with pitch Λ is given by $q\frac{2\pi}{\Lambda}$, with $q = \pm 1, \pm 2, \pm 3, \dots$ [32]. The requirement for coupling to the waveguide mode is that the momentum of the waveguide mode k_{wg} (corresponding to the real part β of the wave vectors k_z calculated in section 2.3) equals the momentum of the incoming light plus the momentum provided by the grating:

$$k_{wg} = k_0 sin(\theta) + q\frac{2\pi}{\Lambda} \tag{2.10}$$

The fact that multiple grating orders are involved allows light of a certain wavelength to couple to multiple modes, as long as Eq. 2.10 is fulfilled. However, the coupling efficiency - defined as the fraction of power radiated in a certain grating order q - generally decreases for higher q [32]. In practice this means that only the first several grating orders allow for efficient coupling to waveguide modes.

Equation 2.10 is used to calculate at which free-space wave vectors light can couple to waveguide modes, assuming a fixed angle of incidence. For a square particle array with pitch Λ, the different grating orders q can be represented by vertical lines of constant in-plane momentum. The diagonal pitch, corresponding to $\sqrt{2}\Lambda$ can be neglected as long as $\vec{E}$ and $\vec{B}$ are aligned with the grating axes. Figure 2.6 shows the same dispersion curves as in Fig. 2.2a, now overlaid with the momentum generated by the different grating orders q (dashed lines) for $\Lambda = 500$ nm under normal incidence ($\theta = 0$). Momentum matching occurs wherever one of the dispersion curves crosses one of the grating orders.
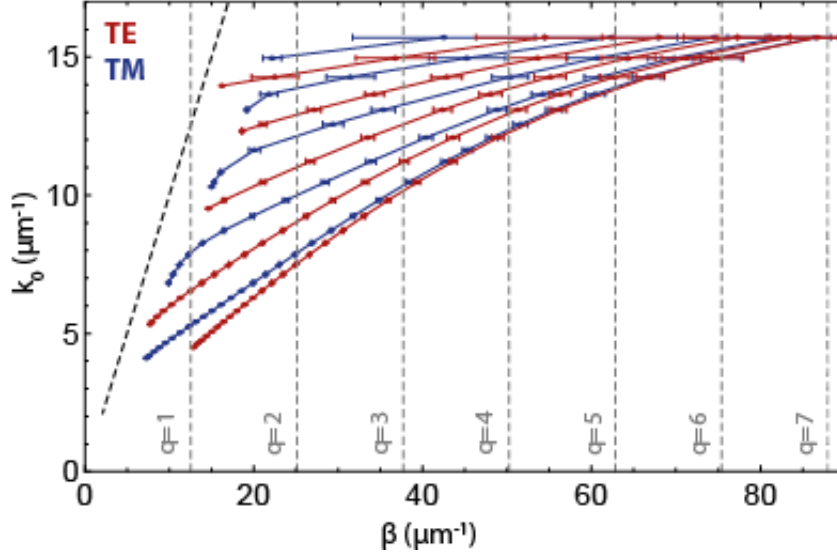
Figure 2.6: *Dispersion curves from Fig. 2.2a together with the momentum generated by the different grating orders q for a grating with 0.5 μm pitch at normal incidence (dashed vertical lines). Momentum matching with one of the modes occurs when its dispersion curve intersects one of the grating orders.*

Since the particle array is two dimensional, the polarization of the light is not relevant under normal incidence. Both the electric field component and the magnetic field component can interact with the particle array. Furthermore, the modes calculated in section 2.3 can propagate both in the z-direction as well as in the x-direction. However, when light illuminates the sample under a non-zero θ, symmetry is broken and the polarization of light becomes important. For light to couple to a mode, the field must overlap with the mode profile as shown in Fig. 2.2b. Thus, in order to couple to the TE modes in the structure, the incoming light needs an in-plane electric field component. Similarly, coupling to a TM mode requires an in-plane magnetic field component. As shown in Fig. 2.5b, p-polarized light has $\vec{B}$ parallel to the surface and has therefore largest mode overlap with the TM modes. Under incident angle θ, the in-plane component of the electric field reduces to $E\cos(\theta)$ and the coupling to TE modes is thus reduced. Reverse arguments hold for s-polarized light. The $\cos(\theta)$ dependence results in the fact that the difference in coupling efficiency for TE and TM modes becomes more pronounced for larger θ.

The principle of momentum matching thus states that light can couple to waveguide modes under the conditions given by Eq. 2.10. As several modes are supported in the waveguide (the number of modes is directly determined by the waveguide thickness) and because multiple grating orders can contribute to the momentum matching, in practice many combinations in the λ_0-θ-plane fulfill Eq. 2.10. To demonstrate this, Fig. 2.7 shows a map of all combinations of θ and λ_0 at which momentum matching is fulfilled for the SOI structure studied here. The lines in Fig. 2.7 are calculated by using the dispersion curves in Fig. 2.6 and the three lowest grating orders ($q = \pm 1, \pm 2, \pm 3$). From this map it can be observed that throughout the entire λ_0-θ-plane it is possible to couple to waveguide modes. The mode density is particularly high at short wavelengths. Not taken into account here is that each mode has a uncertainty in β - as shown in section 2.4 - which causes broadening of the lines in the map, providing an even better coverage of the λ_0-θ-plane. Altogether, Fig. 2.7 shows that coupling to waveguide modes provides an important light trapping mechanism.

2.7 Conclusions

Based on full EM theory, the waveguide modes supported by the SOI wafer used in experiments have been calculated. With these calculations the mode profiles and dispersion curves were obtained. From these calculations it can be concluded that the modes are located inside the active layer and therefore function to enhance the light trapping inside this layer. We showed that absorption broadens the wavelength and angular coupling range to a particular waveguide mode and that the presence of a spacer layer does not significantly changes the wave vectors and mode profiles. Finally it is shown that due to the presence
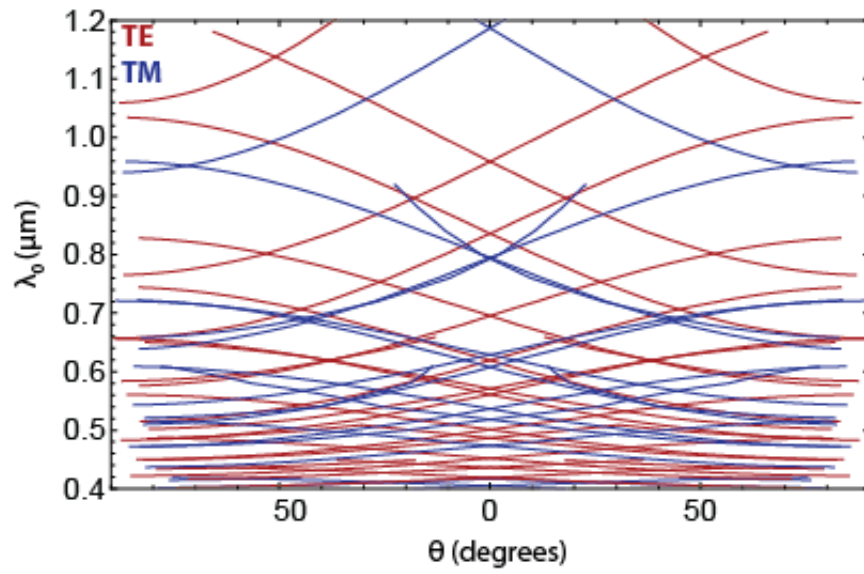
Figure 2.7: *Map of the λ_0-θ-plane relevant for solar cell applications overlaid with the lines where momentum matching occurs with one of the TE modes (red) or TM modes (blue). A high mode density is observed, especially at short wavelength. The fact that so many lines occur throughout the plane indicates that although coupling to waveguide modes is a narrow band feature, it can still have a broadband effect.*

of many modes and grating orders, coupling to waveguide modes can give a broadband effect on the absorption inside the active layer.

Chapter 3

Modeling reflection spectra of patterned SOI wafers and coupling to waveguide modes

3.1 Introduction

To study how light coupling to waveguide modes can be detected in reflection spectra, as well as to study the characteristics of waveguide modes such as spectral width, angular distribution of light and absorption inside thin-film waveguides, detailed information about the interaction of light and the substrate is needed. Finite-element simulations allow the direct study of light-matter interaction both in the far field (reflection and transmission spectra) and in the near field inside the substrate. Here, Finite-Difference-Time-Domain (FDTD) simulations are performed using a commercial software (Lumerical [48]) to systematically study: (1) the influence of Fabry-Perot resonances in the SOI structure and the influence of single particles and particle arrays on the reflection spectra, (2) the influence of coupling to waveguide modes on the absorption inside a SOI waveguide, (3) the spatial intensity and absorption profiles inside the waveguide, (4) the angular distribution of light inside the waveguide, and (5) the normalized scattering cross section of single metal nanoparticles and arrays of silver nanoparticles with and without the presence of a spacer layer. The goal of this simulation chapter is to detect light coupling to waveguide modes and to learn about the influence of particle arrays and spacer layers on the mode coupling mechanism.

3.2 Reflection spectra of patterned SOI wafers

The interaction between metal nanoparticles and waveguide modes in and underlying substrate was first investigated by Stuart and Hall [29]. The main result of this paper is shown in Fig. 3.1. Here, the normalized scattering intensity measured in an integrating sphere for a random array of Ag particles on a silicon-on-insulator substrate, with dimensions indicated in the figure, is shown as a function of wavelength. The graph shows several distinct peaks that the authors attribute to light scattering out of the waveguide due to the metal nanoparticles on top of the waveguide. This experiment shows that there is a strong interaction between metal nanoparticles and waveguide modes in the underlying substrate. The geometry of this experiment will therefore be the starting point of our simulations.

To study the influence of the different layer structures and the presence of particle arrays, we systematically compare the reflection spectra of samples with and without oxide layer, spacer layer and particle array. The reflection spectra for the non-patterned samples are based on Fresnel calculations, whereas the reflection spectra for the patterned samples are produced using FDTD simulations. Periodic boundary conditions are used to simulate an infinite array. A reflection monitor is located above the substrate, which collects all light with a scattering angle $< 90\,^\circ$ with respect to the surface normal. A plane wave source is used with broadband illumination in the visible and NIR part of the spectrum ($300\ \text{nm} \leq \lambda_0 \leq 1200\ \text{nm}$). Optical constants for the calculations were obtained from [46] for Si and [47] for SiO_2. For the simulations, optical constants for Si and SiO_2 were obtained from Palik [49], and a Drude-Lorentz fit to the data from Palik was used for silver. The optical constants for Si and SiO_2 from both references were
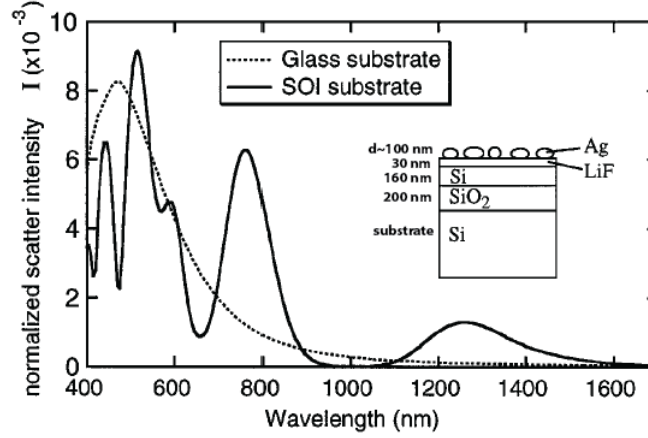
Figure 3.1: *Total reflection measurement as a function of wavelength for a nanopatterned SOI wafer with a 30 nm LiF spacer layer, obtained from ref. [29]. The peaks in the solid line are attributed to light scattering out of waveguide modes supported by the 160 nm Si layer due to interaction with the silver particle array. The sample and its dimensions are shown as an inset.*

compared to check for discrepancies. The deviations in the reflection spectra due to these discrepancies are found to be negligible.

Figure 3.2a shows the broadband reflection spectra of a bare Si substrate (green), a Si substrate with a 30 nm SiO_2 spacer layer (purple), a SOI wafer with a 160 nm Si waveguide and a 200 nm SiO_2 layer (blue), and finally the same SOI wafer with a 30 nm SiO_2 spacer layer on top (orange). Besides
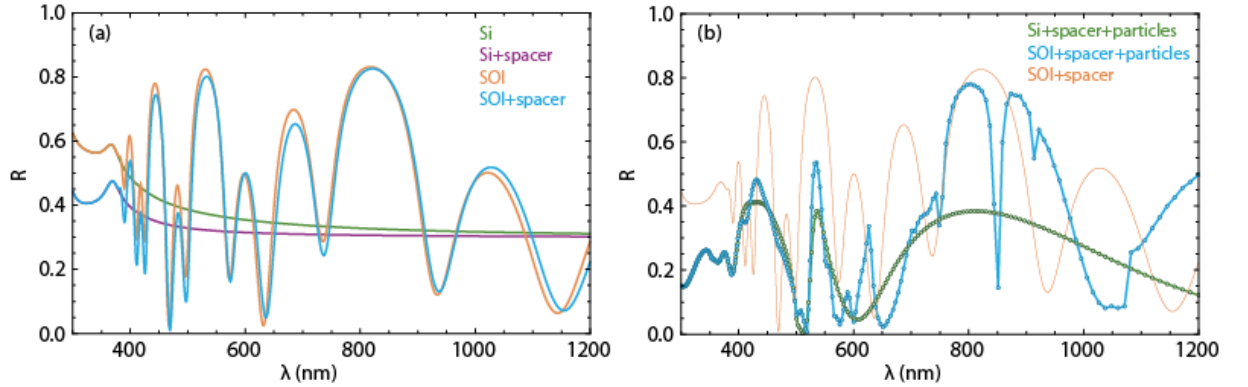

Figure 3.2: *a) Total reflection spectra of a bare Si substrate (green), a Si wafer with a 30 nm SiO_2 spacer layer (purple), a bare SOI wafer with similar dimensions as in the Stuart and Hall experiment (blue), and the same SOI wafer with a 30 nm SiO_2 spacer layer (orange). The spectra are obtained from Fresnel calculations. b) Total reflection spectra of a patterned Si substrate with spacer layer (green), a patterned SOI wafer with spacer layer (blue), and a non-patterned SOI wafer with spacer layer as a reference (orange). These spectra are obtained from FDTD simulations.*

a broadband reflection of $\sim 35 - 40$ %, the bare Si shows only one peak around $\lambda_0 = 380$ nm, which is caused by the local increase of refractive index as a result of the direct bandgap of Si. Comparing this with the purple line shows that the introduction of a spacer layer gives a broadband reduction in reflectivity due to the improved impedance matching as a result of the fact that $1 < n_{SiO_2} < n_{Si}$. The Fabry-Perot resonance in the spacer layer is not observed due to the relatively thin layer with respect to the wavelength.

The reflection spectrum of the bare SOI wafer (blue) shows strong oscillations that become broader for increasing wavelength. These are attributed to the Fabry-Perot effect in the different layers of the SOI wafer. Note that for $\lambda_0 < 390$ nm the reflection spectrum exactly overlaps that of a bare Si wafer as a result of the short absorption length in the top Si layer for these wavelengths. Finally, the presence of a spacer layer on the SOI wafer (orange) again shows a broadband reduction in the reflectivity.

Comparing Fig. 3.2a with Fig. 3.1 shows that the peaks in the reflectivity in Fig. 3.1 are not due to the interaction of waveguide modes and metal nanoparticles on top of the waveguide. In fact, the same peaks are observed in Fig. 3.2a for the bare SOI wafer (with spacer layer), indicating that the peaks stem form a Fabry-Perot effect rather than scattering of light out of the waveguide due to metal nanoparticles. To further prove this point, Fig. 3.2b shows the reflectivity of a Si substrate with spacer layer and a silver metal nanoparticle array on top (green). The spectra are calculated using FDTD simulations. The particles are assumed to be spheres arranged in a two-dimensional array, with a particle diameter of 300 nm and array pitch $p = 500$ nm. The reflection spectrum of the same particle array on top of a SOI wafer with a spacer layer is also shown (blue). The reflection spectrum of a SOI wafer with spacer layer *without* particles (same as blue line in Fig. 3.2a) is shown as a reference in orange.

Comparing the blue line with the orange reference line shows first that the particle array gives a broadband reduction in the reflectivity: the Fabry-Perot peaks in the reflection spectrum are reduced because the particles preferentially scatter the reflected light back into the substrate. Second, the particle array generates enough in-plane momentum to couple light into waveguide modes, resulting in sharp dips in the reflection. Finally, a clear Fano line-shape is observed in the blue line at a wavelength equal to the array pitch ($\lambda_0 = 500$ nm). This is attributed to the interference of the sharp Rayleigh anomaly with the broad particle plasmon resonance [36, 37]. The reflection of the particle array on a Si substrate (green line) confirms several of these observations. First, the sharp peaks in reflectivity at 425 and 540 nm must be a result of the particle array since in the Si substrate a continuous set of waveguide modes is supported instead of a discrete set, and no Fabry-Perot resonances occur. Second, the fact that the sharp dips in the red part of the spectrum do not occur for the thick Si substrate confirms that these are due to coupling to waveguide modes in the thin layers in the SOI wafer. Third, the fact that Fano line-shape at $\lambda_0 = 500$ nm is also observed for the thick Si substrate confirms that it is a result of the interaction between the sharp Rayleigh anomaly and the broad particle plasmon resonance.

3.3   Absorption enhancement and angular the distribution of light in waveguide modes

To prove that the sharp dips in reflection in the blue line of Fig. 3.2b are due to mode coupling, we calculate with FDTD the fraction of the incoming power that is absorbed in the 160 nm Si waveguide. Figure 3.3 shows the absorption in the waveguide (purple) and the reflection (blue) as a function of wavelength. The inset shows the geometry of the sample as used in the simulations. Figure 3.3 clearly shows that all sharp dips in reflectivity in the red and NIR spectral region are accompanied by sharp peaks in the absorption inside the waveguide. This confirms that it is mode coupling that causes that causes these dips in reflection.

Local field intensities and absorption profiles inside the waveguide can also be extracted from FDTD simulations. The absorption per unit volume can be calculated from the local intensity profile, the imaginary component of the dielectric constant, and the frequency: $Abs = -0.5\omega|E|^2\varepsilon''$ [50]. Figure 3.4 shows the field intensity (a and b, color scale) and the absorption per unit volume (c and d, color scale) in a cross section of the waveguide for $\lambda_0 = 914$ nm (a-c) where light couples to a waveguide mode, and for $\lambda_0 = 797$ (b-d) nm where light does not couple to a waveguide mode (see arrows in Fig. 3.3). Each cross section is comprised of three unit cells of the simulation. The waveguide is located between -160 nm $\leq y \leq 0$ nm, and is surrounded by the SiO_2 spacer layer on the top and the 1 μm SiO_2 layer at the bottom. Note that silver particles are located on top of the spacer layer at $x = -500$ nm , $x = 0$ nm and $x = 500$ nm. Figure 3.4b shows how the particles scatter light into the substrate, resulting into a small local intensity enhancement and thereby a small local absorption enhancement (d) at the locations of the particles. (a) shows how light coupling to a waveguide mode propagates through the waveguide in the horizontal direction, resulting into an oscillating intensity profile as a function of x with a wavelength that corresponds to half the inter-particle distance. This is can be attributed to the evanescent tail of the waveguide mode interacting with the particle array, thereby experiencing a periodically changing effective refractive index. This gives rise to the formation of a Bloch-mode. The absorption per unit volume at this wavelength (c) also shows how the absorption is greatly enhanced as a result of light coupling to the waveguide modes. Note that the intensity scale bar of both (a) and (c) are larger than that for (b) and (d); the difference in both intensity and absorption per unit volume for the two cases is an order of magnitude.

Figure 3.4 suggest that light coupling to a waveguide mode propagates in the in-plane direction.
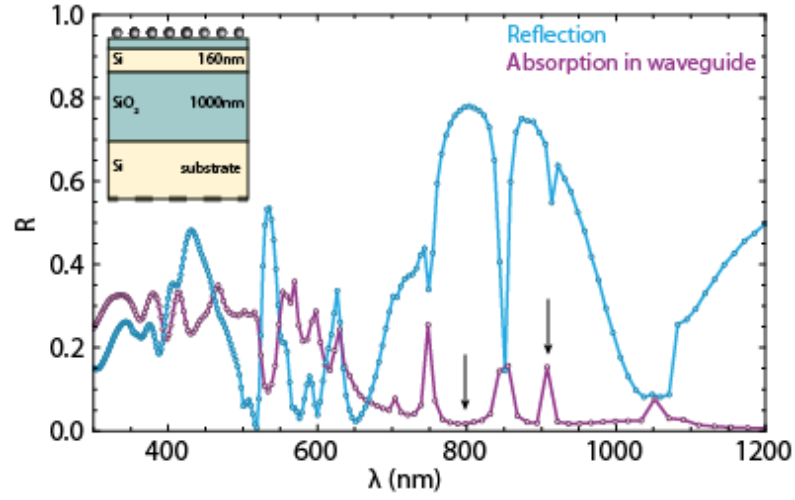
Figure 3.3: *Total reflection (blue) and the absorption inside the 160 nm thick c-Si waveguide (purple). Sharp dips are observed in the reflection spectrum, accompanied by sharp peaks in the absorption in the waveguide that are attributed to light coupling to waveguide modes. The sample used in the simulation is shown as an inset, where the top blue layer is a 30 nm SiO_2 spacer layer and the particles are assumed to be silver spheres with $d = 300$ nm and 500 nm pitch. The small arrows indicate which wavelengths are used for the cross sections in Fig. 3.4.*
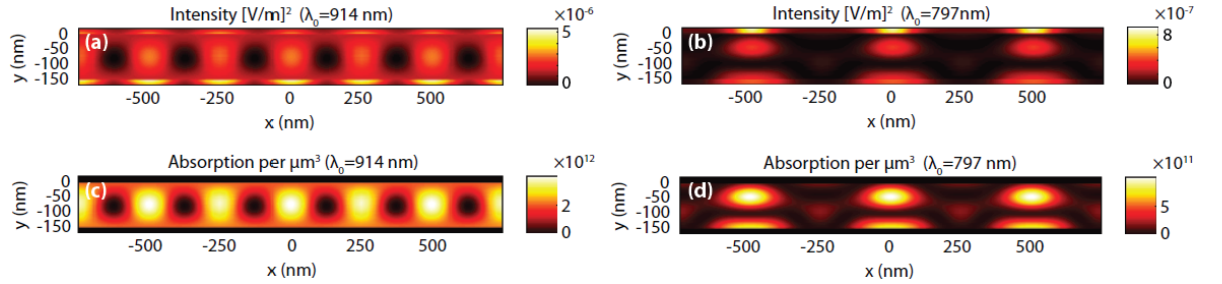

Figure 3.4: *Cross sections of three unit cells of the waveguide (located between -160 nm $\leq y \leq 0$ nm) showing the intensity profiles (a and b) and the absorption profiles (c and d). (a) and (c) correspond to light coupling to a waveguide mode, resulting into light propagating in the in-plane direction. The periodicity of the intensity profile is due to a Bloch mode that is supported by the periodically changing effective refractive index as a result of interaction with the particle array. (b) and (d) correspond to light that does not couple to a waveguide mode, showing scattering of the light into the substrate. Note that the intensity scale bars are different for each figure.*

This can also be studied by calculating the Poynting vector of the light inside the waveguide. A field monitor is placed in the center of the waveguide ($y = -80$ nm), in order to calculate the in-plane and y-component of the Poynting vector at each location in the unit cell. The angle with respect to the $-y$-axis is calculated for all positions and wavelengths. This allows us to determine the normalized angular distribution (weighted for the length of the Poynting vector) for each wavelength, such that integrating over all angles will give 1 for each wavelength. The result is shown in Fig. 3.5. This figure shows that for short wavelengths most power propagates under very small angles. However, for longer wavelengths several very distinct bands can be observed showing a large amount of power propagating under large angles up to $90°$. The spectral location of these peaks corresponds exactly to the location of the dips in reflection and peaks in absorption as observed in Fig. 3.3 (indicated by the arrows), confirming that light coupled to waveguide modes propagates in the in-plane direction. The fact that such modes are not observed for short wavelengths is a direct result of the strong absorption in Si at these wavelengths.
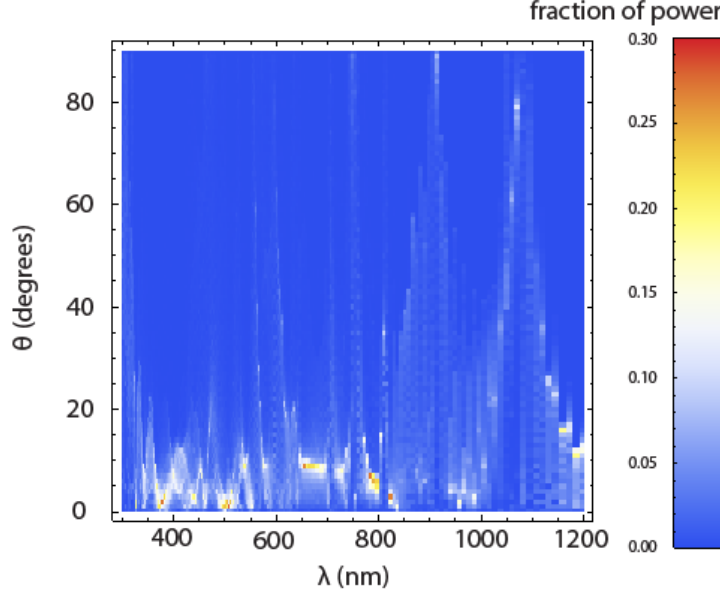
Figure 3.5: *Angular distribution of the Poynting vectors, normalized for each wavelength such that integrating over all angles gives 1 for each wavelength. θ is defined as the angle with respect to the −y-axis. Clear bands with high angles can be observed for longer wavelengths that correspond to light propagating in the in-plane direction as a result of light coupling to waveguide modes.*

3.4 Normalized scattering cross section of metal nanoparticle arrays

For our experiments it is also important to understand how strongly the particle array interacts with incoming light. The simulations so far focused on detecting waveguide modes and comparing the results with the Stuart and Hall experiment. In this section, we use FDTD to calculate the normalized scattering cross section Q_{scat}, defined as the ratio of the scattering cross section and the geometrical cross section $Q_{scat} = \frac{C_{scat}}{\sigma}$, of single particles and particle arrays. Furthermore, it has been shown that the presence of a spacer layer blue shifts the dipole resonance and increases the scattering cross section at resonance [24, 27]. Here, we study this effect as well as the influence of inter-particle coupling on Q_{scat}.

First the scattering cross section of a single particle on a Si substrate with and without a 30 nm SiO$_2$ spacer layer is simulated. The particles are assumed to be a combination of a cylinder with radius $R = 135$ nm and height $h = 70$ nm and two semi-ellipsoidal particles with major radius $R = 135$ nm and minor radius $r = 25$ nm located at the top and bottom. This shape is a good approximation of the actual particle shape obtained in the SCIL fabrication, and the dimensions are those of one of the fields on the samples used in experiments. A sketch of the particle is shown as an inset in Fig. 3.6a, together with a sketch of the simulation setup. For a single particle, the scattering cross section is determined by using a Total-Field-Scattering-Field (TFSF) source, which allows only the scattered light to be transmitted out of the source box. A transmission monitor, located 10 nm outside the source box in the vertical dimension and 20 nm in the horizontal directions (green dashed line), measures the scattered power. Note that the bottom part of this monitor is located inside the Si layer or in the SiO$_2$ spacer layer. In case of the Si substrate a small fraction of the power is absorbed in the thin layer between the TFSF source and the transmission monitor. However, the effect of this absorption on Q is negligible. The simulations were performed with Perfect Matching Layers (PML) at the sides of the simulation box to prevent unphysical reflections, a 10 nm mesh size inside the substrate and in air, a 1 nm mesh size inside the particle and at the interfaces and a 0.5 nm mesh size at the contact point of the particle with the substrate. A broadband source was used with 400 nm $\leq \lambda_0 \leq 2$ μm.

The results are shown in Fig. 3.6a for a sample with (purple) and without (blue) spacer layer. Also shown with arrows is the location of the dipole resonance (d) and the quadrupole resonance (q). It can be observed that the presence of a spacer layer blue shifts the dipole resonance from close to the bandgap of Si at $\lambda_0 = 1100$ nm to $\lambda_0 = 900$ nm such that Q_{scat} has a broad peak in the spectral region where
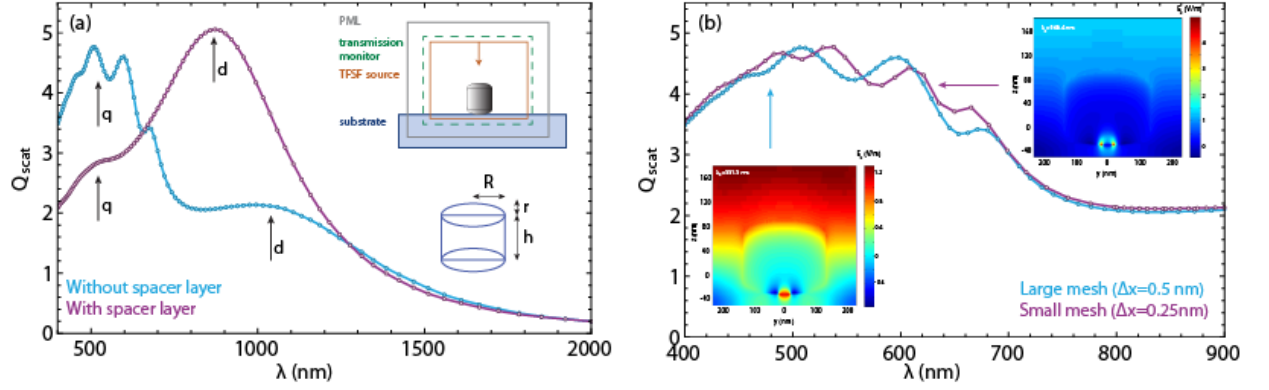
Figure 3.6: *a) Normalized scattering cross section of a single particle on top of a Si substrate with (purple) and without (blue) a 30 nm SiO_2 spacer layer. The arrows indicate the location of the dipole (d) and quadrupole (q) resonance. Both the design of the particle and a sketch of the simulation setup are shown as an inset. **b)** Magnified plot of the small oscillations in Q_{scat} for the sample without spacer layer for a simulation mesh size of 0.5 nm (blue) and 0.25 nm (purple). The change in location and reduction in amplitude of the oscillation for smaller mesh size indicates that the oscillations are a result of hot-spot formation due to the limited mesh size. To further prove this argument, field plots for the two simulations show that the wavelength of the small oscillations reduces for smaller mesh sizes.*

light trapping is most necessary. This is caused by the lower effective index experienced by the near-field of the particle. Furthermore, Q_{scat} at the dipole resonance increases drastically in presence of a spacer layer. Both this blue shift and increase confirms the observations in ref. [24] and [27]. Note that the quadrupole resonance is not shifted and Q_{scat} is significantly reduced at this resonance wavelength due to the spacer layer. The difference with respect to the dipole resonance is caused by the mode profiles of cylindrical particles on a substrate [27]. It has been shown that as a result of symmetry breaking (in presence of a high-index substrate) the field profile of the dipole resonance is strongly localized at the interface such that it is very sensitive to changes in the refractive index of the substrate. On the other hand, the field profile of the quadrupole mode is strongly confined to the top part of the particle. Since the top of the particle is located in air, the quadrupole resonance is not very sensitive to changes in the refractive index of the substrate, and is thus not shifted. This also explains the decrease in Q_{scat} for the quadrupole resonance in presence of a spacer layer. Typically, the quadrupole resonance has poor coupling to far-field radiation. The symmetry breaking as a result of a high-index substrate enhances this radiation. The presence of the spacer layer reduces the effective refractive index, thereby reducing the symmetry breaking and thus reducing the radiation to the far field (lower Q_{scat}). Finally, the dipole resonance is narrower in presence of a spacer layer. The strong localization of the field of the dipole resonance on the interface causes strong coupling to the substrate, resulting into spectral broadening of the resonance. Lowering the effective refractive index by introducing a spacer layer reduces this coupling and thus spectrally narrows the resonance.

The sample without spacer layer shows small oscillations in the quadrupole resonance, caused by hot-spot formation due to the limited mesh size on the metal-air-Si interface at the bottom of the particle. To prove this, the same simulation was performed with an even smaller mesh size of 0.25 nm at the location of the hot-spots. Figure 3.6b shows a magnified plot of Q_{scat} as simulated with a mesh size of 0.5 nm (blue) and 0.25 nm (purple). The shift in wavelength of the small oscillations along with a reduction in amplitude shows that the intensity of the hot spots is reduced and thus that these oscillations are an artifact as a result of the limited mesh size. To further prove this argument, field plots of the particle on Si are shown as an inset for both mesh sizes. These cross sections show E_x as a function of position for $\lambda_0 \sim 550$ nm. Small oscillations in the horizontal direction can be observed where the particle touches the Si interface. Comparison of both field plots shows that the wavelength of the small oscillations reduces for smaller mesh sizes, confirming that the hot-spot formation is a direct result of the mesh size.

To study the effect of inter-particle coupling in a particle array on Q_{scat}, a two dimensional array of the same particles was simulated on a Si substrate with a 30 nm SiO_2 spacer layer. To simulate an infinite array, periodic boundary conditions were used in the in-plane dimensions and PML layers in the vertical dimension. Because a TFSF source can only be used for singe particles, the simulation was run with and

without the particle. The fields (both E and H) of the simulation without the particle were subtracted from those of the simulations with the particle to obtain the scattered field. The Fourier transform of the scattered fields was then used to calculate the Poynting vector in frequency space from which the scattered power can be calculated [51]. The result is shown in Fig. 3.7 where Q_{scat} is shown for a single
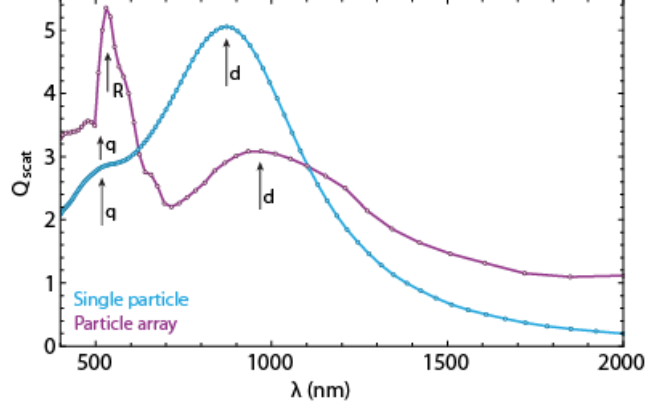

Figure 3.7: *Normalized scattering cross section of a single particle (blue) and a particle array with 500 nm pitch (purple) on top of a Si substrate with a 30 nm SiO_2 spacer layer. The arrows indicate the location of the dipole (d) and quadrupole (q) resonance. The inter-particle coupling lowers the restoring force of the electron oscillation, resulting in a red-shift for the dipole resonance. The collective scattering of in-plane diffracted light (Rayleigh anomaly) causes a sharp peak to occur at the particle pitch, as indicated by the arrow (R).*

particle (blue) and for the particle array with 500 nm pitch (purple). The dipole resonance is strongly reduced and red-shifted as as result of inter-particle coupling. In fact, coupling between the in-plane dipoles moments of the particles lowers the restoring force on the electron oscillation, resulting in a red-shift. Furthermore, a strong and relatively sharp increase in Q_{scat} can be observed for the particle array at $\lambda_0 = 500$ nm. This sharp peak can be attributed to a combination of the broad quadrupole resonance and the sharp peak due to collective scattering from in-plane diffracted light (Rayleigh anomaly). It can easily be shown by using the diffraction equation $nk_{diff} = \frac{2\pi}{\lambda_0}sin(\theta) \pm q\frac{2\pi}{\Lambda}$, that for light under normal incidence the Rayleigh anomaly ($k_{diff} = 2\pi/\lambda_0$) occurs for $n\lambda_0 = \Lambda/q$, such that the first order ($q = \pm 1$) Rayleigh anomaly occurs at $\lambda_0 = 500$ nm. Altogether, these simulations show in which spectral region light will have the strongest interaction with the particle array, as well as the relevance of the presence of a spacer layer.

3.5   Conclusions

FDTD simulations are used to systematically study the effect of particle arrays, spacer layers and substrate configuration on the reflection spectra. This study shows how peaks in reflectivity, that were attributed to particle-waveguide interaction in the Stuart and Hall experiment, are fully caused by the Fabry-Perot effect in the SOI substrate. Furthermore, the fraction of absorbed power, intensity and absorption profiles, as well as the angular distribution of light inside the waveguide are studied to prove that light couples to waveguide modes. We show that mode coupling drastically increases the absorption inside the waveguide and that light propagates in the in-plane direction through the waveguide in Bloch-modes. By studying the amount of scattered light from single particles and particle arrays, the influence of a spacer layer and inter-particle coupling on the scattering cross-section of the particles is determined. The presence of a spacer layer both partially cancels the red-shift due to inter-particle coupling and increases the normalized scattering cross section of the dipole-resonance.

Chapter 4

Spectrally resolved total reflection measurements on patterned SOI wafers

4.1 Introduction

In chapters 2 and 3 we have determined what waveguide modes are supported by the SOI wafer, how light can couple to these modes, and how the coupling can be determined from reflection spectra. In this chapter nano-patterned SOI wafers are fabricated and the total reflection of the different patterns is measured using an integrating sphere. The goal is to experimentally demonstrate light coupling to waveguide modes and compare the data to the insights obtained from simulations. Total reflection measurements are performed to investigate the influence of particle array size and pitch and the presence of a spacer layer on the reflectivity and the efficiency of coupling to modes. The measurements are compared to the calculations performed in chapter 2.

4.2 Methods

4.2.1 Sample Fabrication

A six-inch SOI wafer was used consisting of a 200 nm thick (100) Si layer, on top of a 1 μm thick SiO_2 layer, on top of a (100) Si substrate. On some samples a spacer layer is produced by thermal evaporation of SiO (99.9% pure), resulting into a $SiOx$ layer. The value of x strongly depends on the evaporation speed, giving higher values for x with lower evaporation rates [52, 53]. The deposition is performed at an initial pressure of $p_0 = 3.55 \times 10^{-7}$ mbar and with a deposition rate of ~ 0.5 $\mathring{A}$/s. Using ellipsometry, the thickness is determined to be 33 ± 4 nm and the refractive index $n = 1.7 \pm 0.1$ with negligible absorption ($Im(n) < 10^{-2}$) for $\lambda_0 > 400$ nm. The surface roughness is measured by AFM, and shows an average feature size of $\sigma = 4$ nm.

Silver particle arrays are fabricated on the SOI wafer (with and without spacer layer) using Substrate Conformal Imprint Lithography [39, 40], which allows large-area nanopatterning by using a flexible PDMS stamp to imprint an inverted pattern into a sol-gel layer that is spin-coated onto the wafer. The stamp contains two-dimensional patterns that result into particle arrays with four different particle diameters and two different pitches (500 nm and 700 nm). After drying of the sol-gel and removing the stamp, thermal evaporation of Ag is used to fabricate metal particles inside the imprinted holes. A slow deposition rate was used to form large grains and therefore better particle quality. The deposition is performed under an initial pressure of $p_0 = 1 \times 10^{-6}$ mbar with a deposition rate of ~ 0.5 $\mathring{A}$/s. The height of the particles is directly determined by the Ag layer thickness. The layer thickness was aimed at 125 nm since this was determined to be approximately the optimum to achieve good impedance matching to a Si wafer [25].

The samples were characterized by use of optical microscopy to image the imprint quality, SEM to measure particle diameters and pitch, and AFM to determine the particle height. Both samples with and without spacer layer contained 8 different patterns (2 different pitches, 4 different particles sizes) and
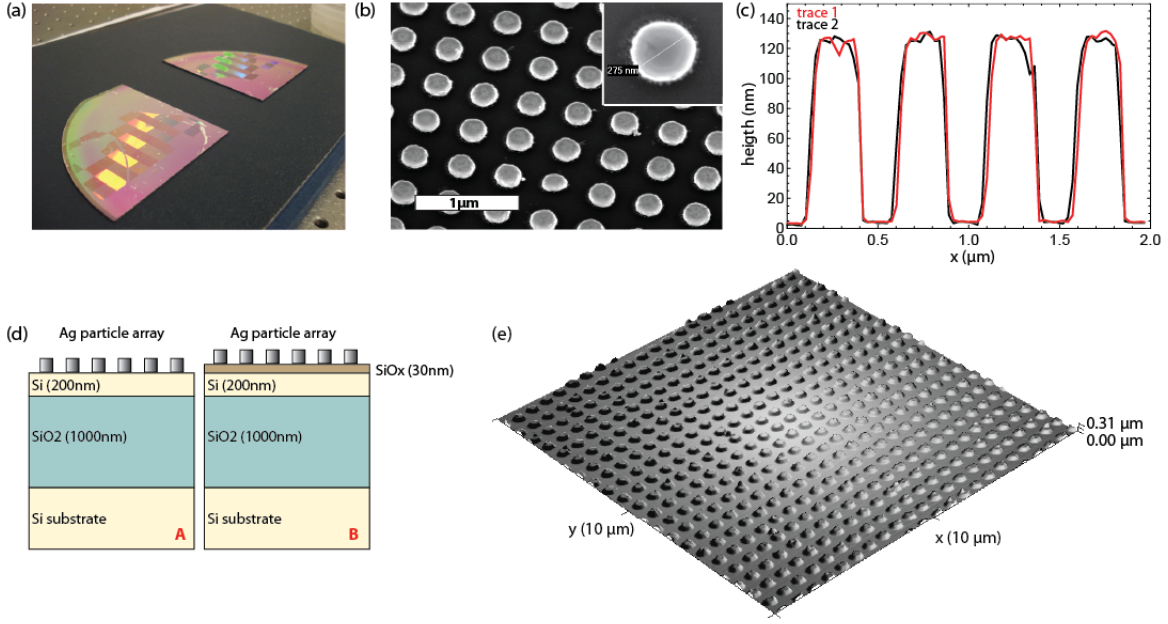
Figure 4.1: **a)** *Photograph of the sample (1 quarter of a 6″ wafer) with (back) and without (front) spacer layer. The squares are fields with different particle pitch and size. The different colors result from Bragg-scattering of light from the silver particle arrays.* **b)** *SEM image of the silver particle pattern on top of the SOI-wafers. The imaged array has a 500 nm pitch and a particle diameter of 275 nm (see inset).* **c)** *Cross sections of two AFM scans showing a particle height of 125 ± 5nm.* **d)** *Schematic cross section of the samples, consisting of a nanopatterned SOI-wafer with and without a 30nm SiOx spacer layer. The particles on top are silver cylinders fabricated with SCIL.* **e)** *AFM image of a 500 nm-pitched particle array showing the large-area reproducibility of the SCIL technique.*

non-patterned reference fields. The fields were repeated at different locations over the sample to obtain some statistics. Figure 4.1a shows a photograph of the two samples, with (back) and without (front) spacer layer. Each square is a 4×4 mm field with a different particle array, slightly varying particle size or particle pitch. The colors originate from diffractive scattering from the particle arrays. In Fig. 4.1b a SEM image is shown of one of the 500 nm-pitched fields, with a particle diameter of 275 nm (see inset). The image shows that the particles are cylindrically shaped and look uniform throughout the array. The particle diameters in the different fields were measured to be $250 - 300$ nm for the 500 nm-pitched fields, and $270 - 330$ nm for the 700 nm-pitched fields. Figure 4.1e shows a 10×10 μm AFM scan, of which Fig. 4.1c shows two cross sections. From this figure it can be observed that the particle height $h = 125 \pm 5$ nm with small variations that are attributed to grain boundaries and small imprint defects. Although SCIL allows large-area patterning (96 4×4 mm fields in this case), the fields are sensitive to damage as a result of fabrication steps or handling the sample during optical measurements. Figure 4.2 shows an example of a field that is damaged, imaged by optical microscopy ($5\times$ magnification) and SEM. Such defects can introduce irregularities in optical measurements as will be shown further on.

The scattering of light from the surface of the samples is strongly dependent on the average feature size, as determined by the intrinsic roughness or array pitch. The Power Spectral Density (PSD) is a commonly used quantity to characterize the surface morphology of thin films [54, 55]. It is a power spectrum of the feature size on the surface of the sample and is directly related to the amount and angular distribution of light scattered from the surface [56]. The discrete two-dimensional PSD can be calculated from the AFM data according to [56]

$$PSD(f_x, f_y) = \frac{1}{L^2} \sum_x \sum_y (h_{xy} e^{-2\pi i (f_x x + f_y y)} \Delta x \Delta y)^2 \tag{4.1}$$

where L is the scan size, h_{xy} is the height profile from the AFM data, f_x and f_y are the spatial frequencies in the x and y dimensions respectively, and Δx and Δy are the step sizes in each direction. Due to the discrete nature of the AFM scans and its finite size, Eq. 4.1 is only valid for spatial frequencies ranging from $1/L$ to $1/\Delta x$. Peaks in the PSD represent the main spatial frequencies in the pattern, and thus
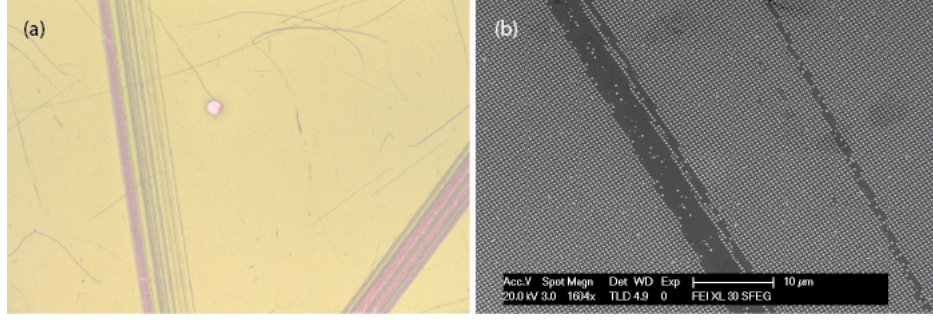
Figure 4.2: a) *Optical microscope image (5× magnification) of a silver particle array that is damaged by scratches.* **b)** *SEM image of a typical scratch in the pattern. Several lines of particles are removed from the array.*

provide a direct measure of the in-plane momentum that incident light can obtain, by scattering from these structures. For example, a peak in the PSD at f_x means that light can obtain an in-plane momentum of $2\pi f_x$. Figure 4.3 shows the two dimensional PSD (color scale) obtained from an AFM scan on a 500 nm-pitched field. A clear peak is observed at $f_x \sim f_y \sim 2 \ \mu m^{-1}$, as expected. The small mismatch with respect to $f_x = f_y = 2 \ \mu m^{-1}$ is a result of a small rotation of the AFM scan with respect to the array axes. The PSD integrated over one dimension is shown in the inset of Fig. 4.3. The small oscillations on the sides are a result of the fact that the PSD is a Fourier transform over a limited spatial range. This results into small oscillations according to a sinc-function centered around the peak.
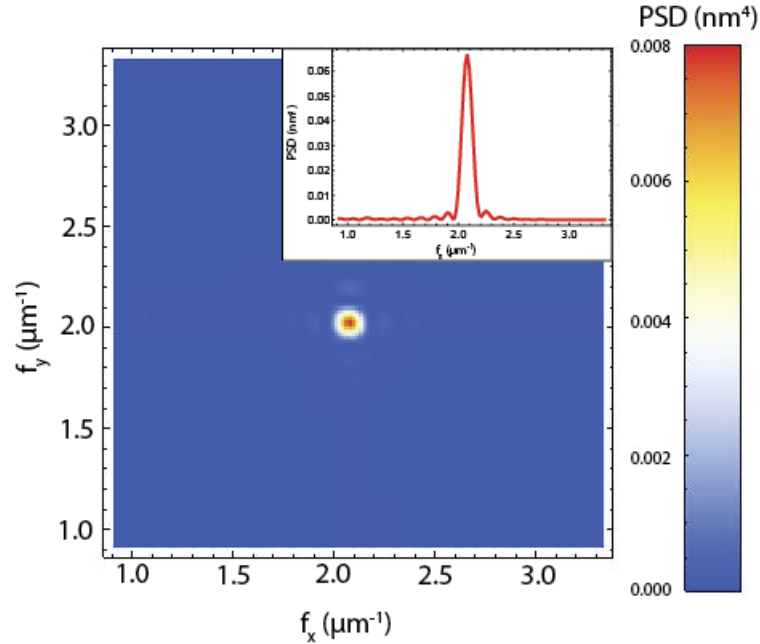

Figure 4.3: *Power spectral density of one of the 500 nm-pitched fields, showing a peak at $f_x \sim f_y \sim 2 \ \mu m^{-1}$. The small mismatch with respect to $f_x = f_y = 2 \ \mu m^{-1}$ is a result of a small rotation of the AFM scan with respect to the array axes. The inset shows the one dimensional PSD, obtained from the 2D version by integrating over the f_y dimension.*

4.2.2 Setup and Measurements

Total reflection measurements were performed using an integrating sphere. Due to the highly reflective internal surface of the sphere, not only the specular reflection but also all the diffuse reflection is collected. Only light leaking out through the entrance hole is not collected. This principle is shown in Fig. 4.4a. The samples were illuminated using a pulsed (20 MHz, ~ 5 ps pulse width) supercontinuum broad-band source (Fianium, model SC400-2) under an angle of incidence close to normal incidence ($\theta \sim 3\,^\circ$). The

pump power $P \sim 2$ W and the wavelength range 420 nm $< \lambda_0 < 2$ μm; the light is unpolarized. A gold coated integrating sphere is used which has high reflectivity in the NIR/IR spectral range. Light was collected with a multi-mode fibre and analyzed by a spectrometer with a NIR grating (Ocean Optics, USB4000, grating 4). This allows efficient detection of total reflection in the range of 600 nm $\leq \lambda_0 \leq 975$ nm. A x-y-z-translations stage along with a rotation stage is used to position the sample as close and flat as possible to the port of the integrating sphere without touching it. Although perfect closure was not possible, this setup allowed us to minimize the spacing between the sample and the port of the sphere to be < 0.5 mm. Leakage from the small slit is expected to be smaller than the measurement error. A sketch of the setup us shown in Fig. 4.4b and a photograph of the integrating sphere and sample stage is shown in Fig. 4.4c.
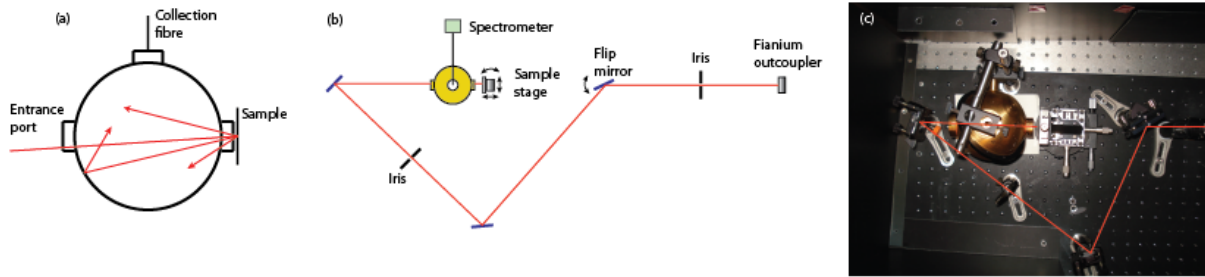

Figure 4.4: *a) Principle of an integrating sphere: all light reflecting from the sample bounces around in the sphere until is is collected by the collection fibre. Only light leaking out of the entrance port is not collected. b) Sketch of the setup used to measure total reflection. c) Photo of the integrating sphere and sample stage.*

The spectrum of a gold reference surface is used to calibrate the reflectivity measurement - using optical constants for Au from Johnson & Christy [57]. An integration time of 100 ms was used. A background signal of ~ 1300 counts was subtracted from both the measured signal and the reference signal. Measurements on fields with a similar pattern were averaged to yield a characteristic spectrum for each pattern.

4.3   Results and Discussion

In this section, the influence of particle size, pitch and presence of the spacer layer on the reflection spectra is studied. In Fig. 4.5 the total reflection spectra for particle arrays with 700 nm pitch (a,b) and 500 nm pitch (c,d) are shown. Data for different particle size are indicated in each graph. Data are shown for the sample with (b,d) and without (a,c) spacer layer. The spectrum of a reference field (no particles) is also shown (gray). We first describe the details for the reference spectra. These show a smooth oscillatory behavior with maxima at 640, 740, and 870 nm that are attributed to Fabry-Perot resonances in the SOI layer structure. Data on the reference fields with and without spacer layer show the same qualitative trends. Similar trends were observed earlier by Stuart and Hall [29] and attributed to light scattering out of waveguide modes from metal particle arrays. The fact that the oscillations are also present in the reference samples, without particles, indicates they can be fully attributed to Fabry-Perot effects. In each of the panels (a-d) data are shown for different particle diameters (colors); they are quite similar. A large difference in the spectra is observed for different particle pitch (compare (a)-(c) and (b)-(d)). First of all, the presence of the spacer layer causes a broadband reduction in reflectivity, as expected from the better impedance-matching between air and Si. The particle array causes distinct dips in the reflectivity that occur at 890 nm. For the 500 nm pitch, more dips are observed at 920 nm and at 630 nm, while the reflectivity is increased at 740 nm and in the $810 - 900$ nm spectral band.

From chapter 3 we know that light coupling to waveguide modes can be recognized by well pronounced dips in the reflection spectrum, that are most pronounced at longer wavelengths due to the large propagation length of the modes. The number of available waveguide modes is merely determined by the layer structure, while the particle array on top determines to which mode light can couple most efficiently. From the various dips observed in Fig. 4.5 it is clear that strong mode-coupling occurs at several wavelengths, depending on the particle pitch. Coupling to waveguide modes is most efficient for the 500 nm pitched fields, as it follows from the deep dips in the reflection.
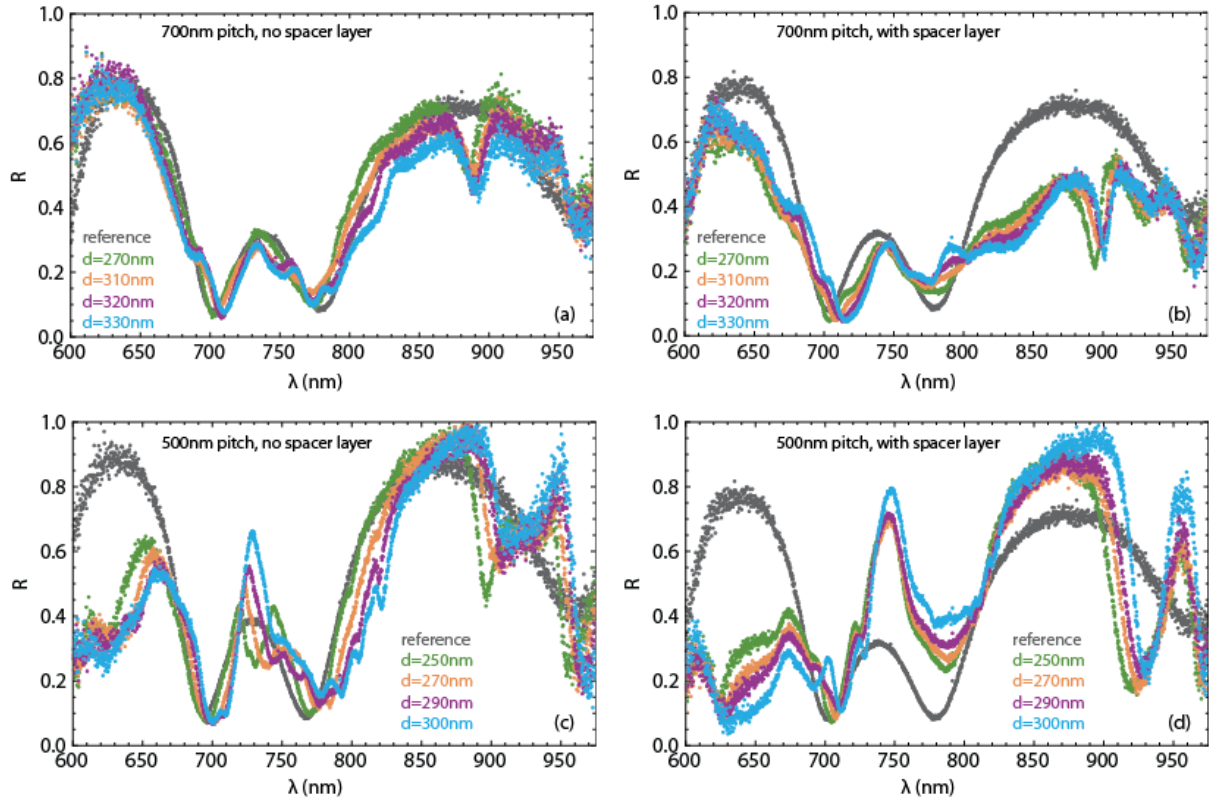
Figure 4.5: *Total reflection measurements showing the influence of the pitch (500 nm and 700 nm) and four different particle sizes for each pitch (color). The spectra are compared to non-patterned reference fields (gray).* **(a)** *and* **(b)** *represent the 700 nm pitched fields,* **(c)** *and* **(d)** *the 500 nm pitched fields.* **(a)** *and* **(c)** *show the fields without spacer layer,* **(b)** *and* **(d)** *the fields with spacer layer.*
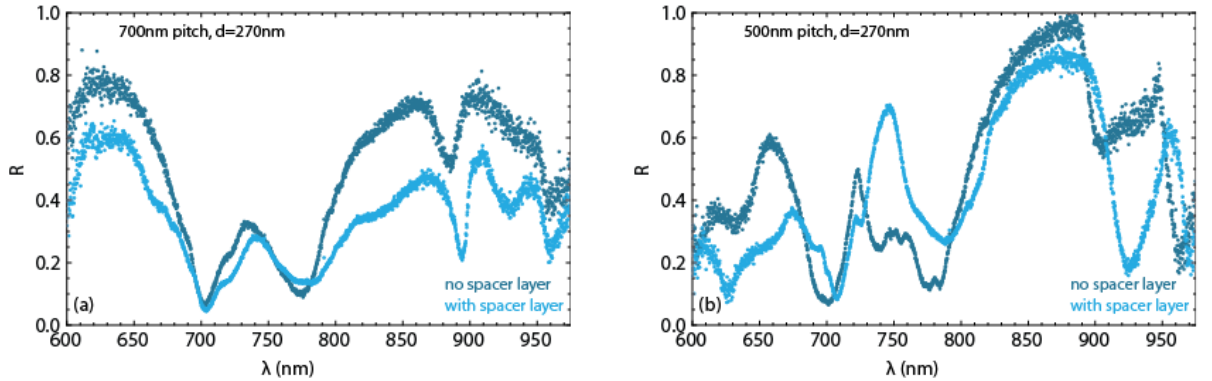
Figure 4.6: *Total reflection measurements of samples with (light blue line) and without (dark blue line) a spacer layer for a 700 nm pitched field* **(a)** *and a 500 nm pitched field* **(b)**. *The particle size is the same for all four measurements (d = 270 nm). The sample with spacer layer shows more pronounced dips in the reflection spectrum as a result of more efficient coupling to waveguide modes.*

The influence of the spacer layer on the coupling to waveguide modes can be investigated in more detail using Fig. 4.6. Here, the reflection spectra for a 700 nm pitched field (Fig. 4.6a) and a 500 nm pitched field (Fig. 4.6b) with (light blue) and without (dark blue) are shown for the same particle size ($d = 270$ nm). From Fig. 4.6 it can be seen that besides a slightly lower overall reflection, the presence of the spacer layer results into more dips than without the spacer layer. In Fig. 4.6a this is most pronounced for $\lambda_0 > 900$ nm where an extra dip is observed at $\lambda_0 \sim 930$ nm. Similarly, Fig. 4.6b shows that the dips in reflection at $\lambda_0 \sim 630$ nm and $\lambda_0 \sim 920$ nm are much deeper for the sample with a spacer layer. The

enhanced coupling is attributed to the enhanced normalized scattering cross section of the particles with the spacer layer: as shown in chapter 3, introducing the spacer layer causes a blue shift in the location of the dipole resonance from the IR to the NIR as well as increases the normalized scattering cross section in the NIR, which is due to the enhanced driving field at the particles [24].
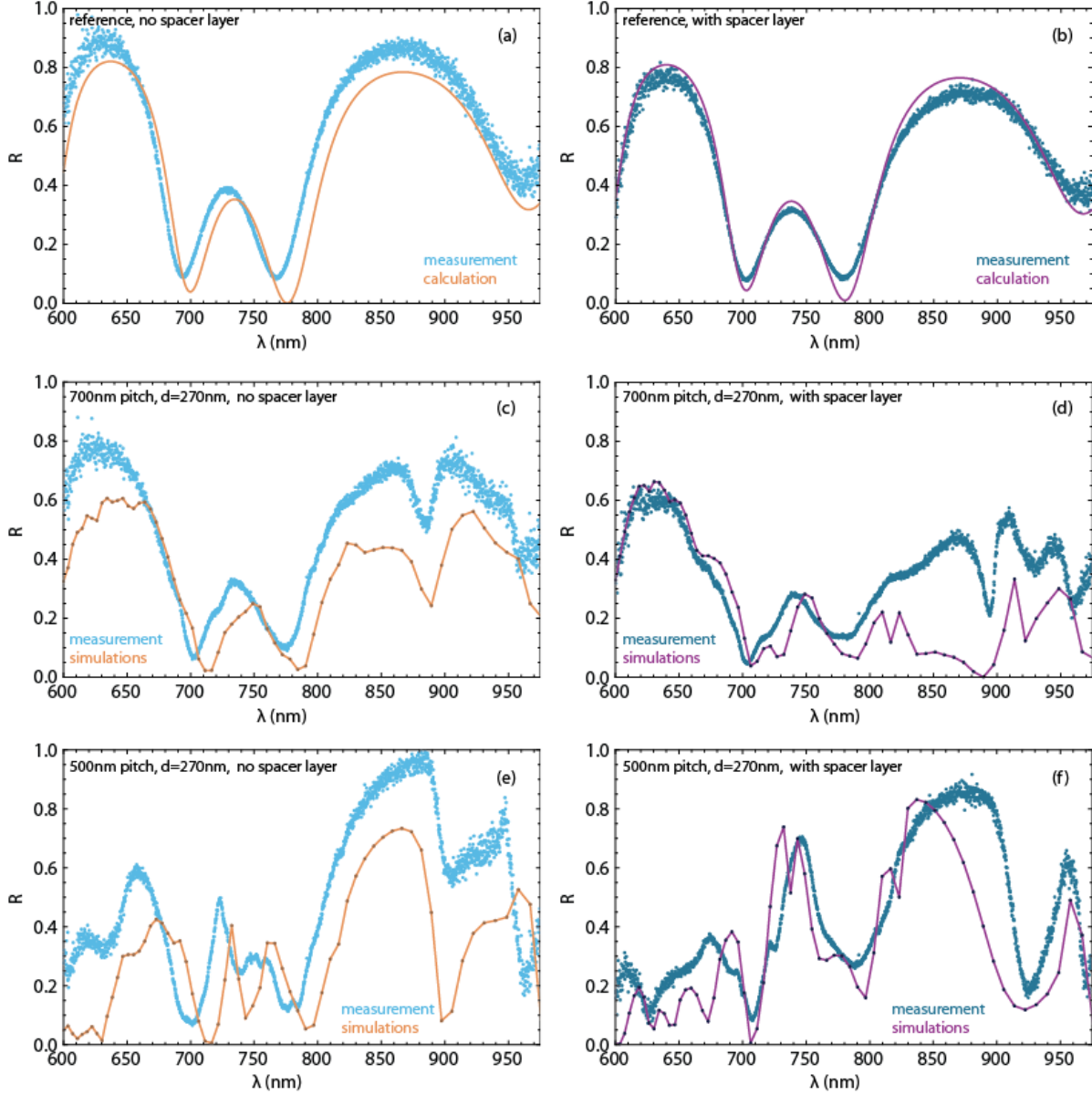

Figure 4.7: *Comparison between total reflection spectra from measurements (blue lines) and calculations/simulations (orange and purple lines), for the sample without spacer layer (left column) and with spacer layer (right column). (a) and (b) represent the non-patterned reference fields, (c) and (d) the 700 nm pitched array, and (e) and (f) the 500 nm pitched array. All measurements for the sample without spacer layer show a small horizontal shift with respect to the simulations. The wavelength at which mode coupling occurs compares well between experiment and theory.*

In Fig. 4.7 the measured reflection spectra are compared to calculated and simulated reflection spectra. Fresnel calculations were used for the unpatterned samples, FDTD simulations for the patterned samples. The left column corresponds to the sample without a spacer layer, the right column to the sample with spacer layer. Figures (a) and (b) show the non-patterned reference fields. The measurements give good correspondence to the calculations, except for a small horizontal shift for the sample without spacer layer. This deviation will be discussed in more detail below. Figures (c-f) correspond to the measurements and simulations of a 700 nm and 500 nm pitched field with a particle diameter of $d = 270$ nm, with and without

spacer layer. The simulations show a qualitative match to the measured spectra, while the simulations show a lower overall reflection than the measurements. In Fig. 4.7d for the 700 nm pitch with spacer layer, a larger discrepancy is observed between simulations and measurements in the wavelength range above 800 nm. For the 700 nm pitch sample without spacer layer, a similar horizontal shift is observed as for the 500 nm pitch sample without a spacer layer. Finally, the simulations show deeper mode-coupling dips for the 500 nm pitched fields than the 700 nm pitched fields in agreement with the measurements.

The deviations between measurement and simulations may can be attributed to differences in optical constants, layer thicknesses, particle geometry, defects in the particle array and dust particles present on the array. The wavelengths of the mode-coupling dips correspond very between the measurement and theory. Because of this good qualitative agreement, further simulations can be used to find the optimal design for the particle array for optimized coupling to waveguide modes.
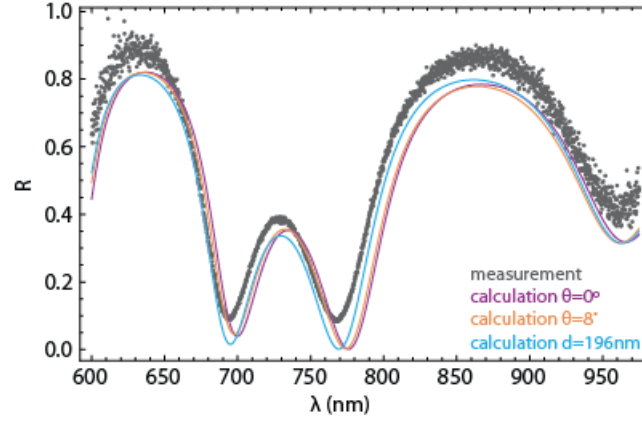

Figure 4.8: *Total reflection measurement for a non-patterned reference field without spacer layer (gray), along with calculated reflection spectra for normal incidence (purple), $\theta = 8\,°$ (orange), and normal incidence but with a 4 nm deviation in waveguide layer thickness (blue). This shows that the horizontal shift, as observed for the sample without spacer layer in Fig. 4.7, can be explained by a small deviation in waveguide layer thickness of merely 2%.*

The non-patterned reference field without spacer layer was used to investigate the cause of the horizontal deviation between the calculations and measurements. The shift can have several causes. First, the calculations assume normal incidence whereas the measurements were performed with $\theta \sim 3\,°$. Figure 4.8 shows the measured data as presented in Fig. 4.7a in gray, together with the calculations at normal incidence (purple) and the calculations for $\theta = 8\,°$ (orange). The figure shows that the difference in angle of incidence does not explain the horizontal shift since the purple and orange line almost overlap. A second cause can be a minor deviation in the layer thickness of the waveguide with respect to the suppliers' specifications. To check this, the reflection spectrum from a SOI wafer with a waveguide thickness of 196 nm is shown as a blue line in Fig. 4.8. This line shows that a reduction in layer thickness of only 4 nm (corresponding to merely 2 %) explains the horizontal shift.

Finally, the measurements can be compared to the calculations from chapter 2. Based on the dispersion curves and the momentum generated by the grating, it can be calculated at what wavelengths momentum matching occurs for light under normal incidence. Under these conditions, light can couple to both TE and TM waveguide modes since the mode overlap is similar for TE and TM polarization in case of normal incidence. In Fig. 4.9, the dispersion relations of a 700 nm pitched field (a) and a 500 nm pitched field (b) are shown for the sample with spacer layer. The gray vertically dashed lines correspond to the momentum generated by the different momentum orders q under normal incidence. The wavelengths of the dips are determined by fitting a Gaussian to the measured data, and are shown as green horizontal lines. As mentioned in section 2.6, momentum matching occurs when the dispersion curve of a mode crosses one of the vertical dashed lines. From both Fig. 4.9a and b it can be seen that the green horizontal lines all occur at values for k_0 where one of the dispersion curves intersects with one of the vertical dashed lines (green dots). Note that some green lines intersect with two cross sections of the dispersion curve with the grating orders. At these wavelengths momentum matching with two waveguide modes occurs simultaneously, which can give rise to broader dips in the reflection spectra. The fact that all green lines cross the cross sections of the dispersion curves with the grating order lines means that the measurements fully confirm the predictions of the calculations from chapter 2. Note that small deviations
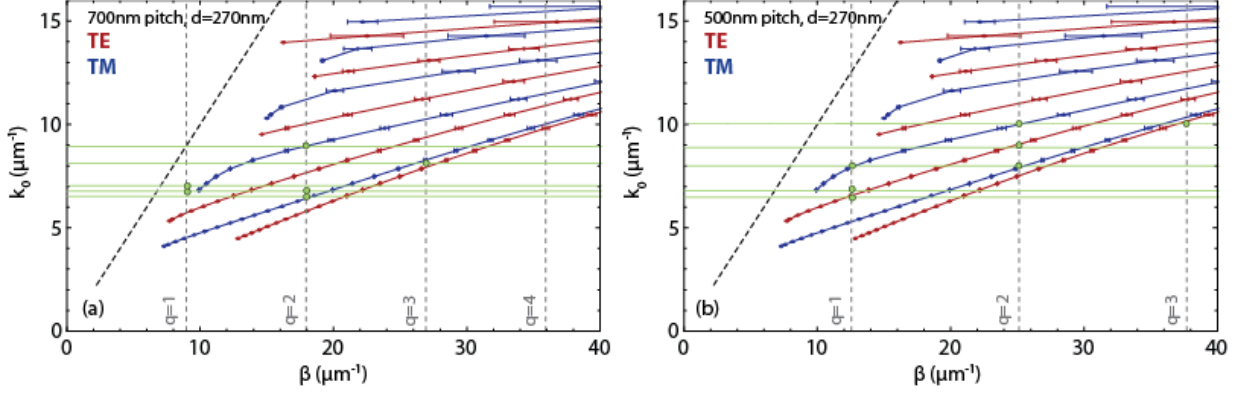
Figure 4.9: *Comparison between the dispersion curves as calculated in section 2.3 and the measurement (green horizontal lines), for a 700 nm pitched field (**a**)) and a 500 nm pitched field (**b**)). Both samples include a SiO_x spacer layer. The locations of the green lines correspond to k_0 values where momentum matching occurs between the dispersion curves and the momentum generated by the grating (gray vertically dashed lines).*

can be accounted for as well as small deviations in layer thickness, optical constants and the non-zero angle of incidence used in the measurements ($\theta \sim 3°$).

4.4   Conclusions

Using an integrating sphere, total reflection measurements were performed on SOI wafers with different particle array designs. By comparing the reflection spectra it is concluded that the particle size only has a small effect on the overall reflectivity of the samples. The array pitch is shown to have a large influence on the total reflectivity as well as on the ability for light to couple to waveguide modes. This is consistent with the view that the particle array functions as a two dimensional grating, of which the pitch determines at which wavelength coupling to waveguide modes occurs. Furthermore it is shown that the presence of a spacer layer reduces the overall reflectivity and increases the coupling efficiency to the waveguide modes. Good agreement is found between measurements and FDTD simulations and simulations can thus be used to further optimize the particle array design. The dips observed in the total reflection measurements correspond well to calculated wavelengths at which mode coupling occurs. This would directly demonstrates how the coupling of incident light to waveguide modes is dependent on array pitch and spacer layer and serves as a guide how to design further optimized scattering geometries.

Chapter 5

Angle-resolved photoluminescence and specular reflection of Erbium doped waveguides

5.1 Introduction

The spectrally resolved total reflection measurements discussed in chapter 4 have shown that light coupling to waveguide modes can be detected experimentally, and very good correspondence between the measurements and calculations has been observed. However, measuring dips in reflection does not conclusively proof that the light is absorbed in the waveguide. Light can also be absorbed in the underlying substrate or in the metal particles, the latter being enhanced by the Rayleigh anomaly [38]. To prove that light is actually absorbed inside the waveguide, we present a new method to probe the intensity enhancement inside thin-film semiconductor layers. Angle-resolved photoluminescence (PL) of optically active erbium ions implanted inside the waveguide is used to prove that light couples to waveguide modes. This is compared with angular resolved specular reflection measurements to investigate the angular dependence of the waveguide coupling mechanism.

5.2 Theory

Erbium is a rare-earth element which in pure form is a metal. When implanted into a dielectric or semiconductor it generally assumes a trivalent charge state with the electronic configuration $[Xe]4f^{11}$ [41]. Due to the spin-spin and spin-orbital interactions between the electrons in the 4f shell, the different 4f energy levels are separated by large energy differences. Fig. 5.1, obtained from ref. [58], shows a sketch of the energy levels of Er^{3+}, both as a single ion and as implanted in a solid material. The Stark effect as a result of the static electric field due to the atomic charges of the host material causes the degenerate energy levels to split. The internal 4f shell atomic transition from first excited state $^4I_{13/2}$ to the ground state $^4I_{15/2}$ causes 1.53 μm emission [59]. Due to the luminescence in the IR, where many materials including Si are transparent, erbium has been recognized as a useful emitter that can be used in many host materials. Previous work has investigated PL of erbium implanted in Si-nanocrystals in SiO_2 [60], dielectric and semiconductor materials [41, 58] or combinations thereof [60], and many thin photonic materials [58], focusing both on fundamental excitation mechanisms [61] and on the use of erbium as a gain medium or to probe the local optical density of states [62].

For Er-doped crystalline Si it was found that co-implanting O ions is beneficial for many reasons [59]: the presence of O ions (1) increases the solubility of Er in Si, (2) increases the PL signal, (3) reduces temperature quenching, and (4) inhibits Er segregation during solid phase epitaxy by changing the chemical surrounding. Many studies have confirmed that co-implanting O ions along with Er ions allows efficient luminescence centers to form, which are located 0.15 eV below the c-Si bandgap [58, 59, 61]. To efficiently create these luminescence centers in Czochralski Si, 6 oxygen atoms are needed per Er ion [61]. Furthermore, the ion implantation process causes severe damage to the crystalline structure of a c-Si host. Annealing the samples at $\sim$ 620 °C for 30 minutes to several hours induces epitaxial recrystallization of
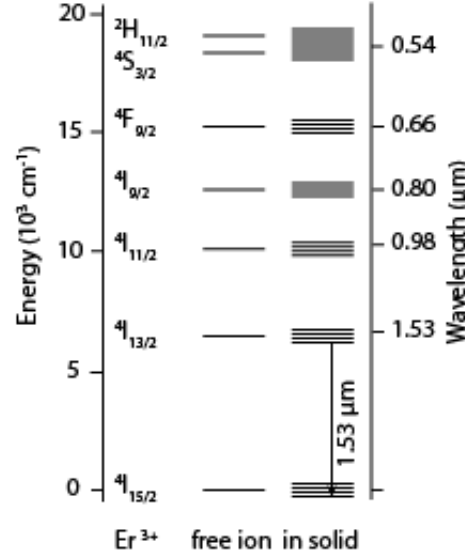
Figure 5.1: *Energy levels of the trivalent charge state, shown for a free ion (left) and for an ion inside a solid host crystal lattice (right) resulting into Stark splitting of the degenerate energy levels. The energy of the different states is shown on the left axis, the corresponding wavelength on the right axis. The figure is obtained from ref. [58].*

the c-Si, and annealing around 1000 °C for 30 seconds to one hour activates the dopants and reduces the residual defect density [59]. The latter annealing step also allows efficient formation of Er-O luminescence centers. The location just below the Si bandgap allows efficient excitation of Er due to the fact that the Er ions can either be pumped directly or via carrier mediated excitation [58]. The latter refers to the transfer of excitons from the Si to the luminescence centers located inside the Si. By comparing erbium PL in different host materials it has been shown that even at a pump wavelength of 980 nm the excitation of erbium is dominated by the carrier mediated mechanism [58]. This can easily be seen by considering the effective absorption coefficient of the direct excitation of the erbium ions and the absorption coefficient of silicon. Doping the 200 nm thick Si waveguide with 1×10^{15} ions/cm^2 yields an effective ion density of 5×10^{19} ions/cm^3. With a scattering cross section of 1×10^{-21} cm^2/ion [63], the effective absorption coefficient of the erbium in the waveguide is $\alpha_{Er} = 5 \times 10^{-2}$ cm^{-1}. On the other hand, the absorption coefficient of silicon at $\lambda_0 = 0.98$ μm is $\alpha_{Si} = 1.07 \times 10^2$ cm^{-1} which is four orders of magnitude larger than the direct absorption coefficient. Due to thermalization to the Si bandgap the PL signal is strongly quenched. In fact, quenching can occur via two mechanisms [58]: (1) through dissociation of the electron hole pair before the transfer to Er takes place, or (2) non-radiative decay of the excited Er ion. Both require interactions with phonons, giving rise to more quenching at higher temperatures. This temperature dependent quenching causes the PL intensity to be two orders of magnitude higher when the sample is cooled below 100 K [58]. Co-doping with O ions reduces this difference to roughly one order of magnitude.

5.3   Methods

5.3.1   Sample Fabrication

A similar SOI wafer as described in section 4.2.1 was used. Before further processing, ion implantation was performed by the University of Surrey Ion Beam Centre. As mentioned in section 5.2, the local O density has to be 6 times the local Er density to effectively fabricate Er-O luminescence centers. The implantation recipe has been determined using atomic collision based Monte Carlo simulations performed with SRIM software [64]. Erbium was implanted at 281 keV and a total fluence of 1×10^{15} cm^{-2}, obtaining a depth profile with a peak density at 100 nm depth, corresponding to the center of the waveguide. The oxygen was implanted at 40 keV and a total fluence of 1×10^{16} cm^{-2}, also obtaining a peak density at 100 nm depth. The density profiles as a function of depth, obtained from SRIM simulations, are shown in Fig. 5.2, where the red line corresponds to the Er ions, the dashed black line to the minimum O density

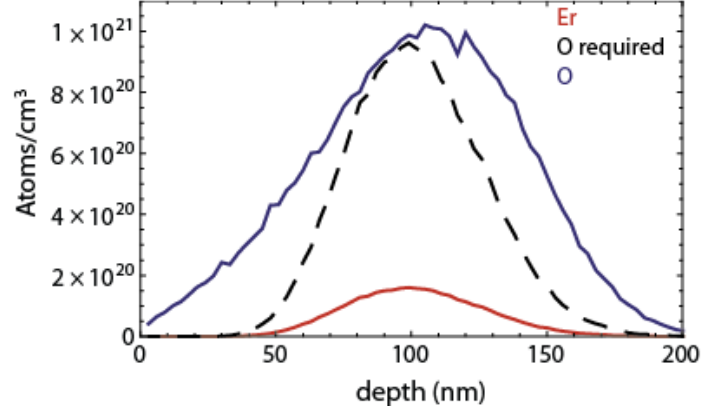required to efficiently produce luminescence centers, and the blue line to the obtained local O density.

Figure 5.2: *Depth profiles as determined by SRIM software, showing the local density of: Er (red), the required O to obtain efficient luminescence centers (dashed black) and the actual O (blue). The distributions peak at the center of the waveguide (depth= 100 nm).*

The ion implantation process destroys the crystalline structure of the Si top layer, causing it to become amorphous. This is clearly visible in Fig. 5.3a where the gray circular area was exposed to the ion beam. Due to the strong absorption in a-Si, the red color as a result of the Fabry-Perot effect is no longer observable. Ellipsometry is performed on the implanted area to determine the optical constants. Figure 5.3c shows η (blue) and κ (red) as a function of wavelength along with the model optical constants for a-Si from literature [49]. Despite the noise for $\lambda_0 > 600$ nm, the overall trend shows good comparison with the model, indicating that the gray area is amorphous. After the implantation, the sample was annealed at $680\,^\circ$ C for 30 min under N_2 to induce the epitaxial recrystallization of the amorphous Si waveguide. Additionally, the sample was annealed in a rapid thermal annealer (RTA) for 2-3 min at $900\,^\circ$ C under a N_2 flow to activate the dopants as well as to reduce the remaining defect density. Figure 5.3c shows a photograph of the sample after annealing, showing how the a-Si has crystallized and the red color as a result of the Fabry-Perot effect is visible again. To investigate if the annealed material corresponds to c-Si, ellipsometry is also performed on the annealed region. Figure 5.3d shows the optical constants (red and blue) along with the model optical constants from literature [46] (gray dashed and black dashed). The good correspondence shows how well the recrystallization has repaired the crystalline structure, such that we assume that the Er-implanted and annealed waveguide is fully crystalline.

The fabrication of the SiO_x spacer layer as well as the silver nanoparticle arrays is performed similarly as described in section 4.2.1. The spacer layer thickness was determined using profilometry as well as ellipsometry. SEM characterization shows that the particles have a "donut" shape (Fig. 5.4a). To determine the thickness of the different layers in the SOI wafer, a cross section was made using Focused Ion Beam (FIB) milling. Fig. 5.4b shows a SEM image of the cross section milled with a gallium ion beam (30 kV, 0.28 nA), taken under a $52\,^\circ$ angle. The layer thicknesses are 1.03 μm for the oxide layer, 197 nm for the Si waveguide, and 76.1 nm for the spacer layer. Except for the spacer layer, these thicknesses correspond well to the specified thicknesses, which were used in calculations and simulations. The measurement of the thickness of the spacer layer has a large uncertainty due to the fact that milling was performed with a relatively high current resulting into edges that are not sharp. Therefore, the top of the layer is difficult to recognize.

5.3.2 Measurement geometry

A schematic of the setup used for the PL measurements is shown in Fig. 5.5. Two different pump wavelengths were used, each corresponding to an absorption transition of erbium (see Fig. 5.1). An argon gas laser was operated at the $\lambda_0 = 488$ nm line (Coherent Innova 90) with a maximum output power of ~ 300 mW and a $100 : 1$ power ratio as a function of polarization. The other pump laser is a $\lambda_0 = 980$ nm diode laser (Roithner, LDM980/25LT) with a maximum power output of 25 mW. By the use of a flip mirror, the 488 nm beam could be used to illuminate the sample either through a free-space path yielding high pump power but fixed angle of incidence, or through a fibre coupled path yielding lower pump powers but varying angle of incidence. A 25x objective with NA= 0.5 (Melles Griot) was used to
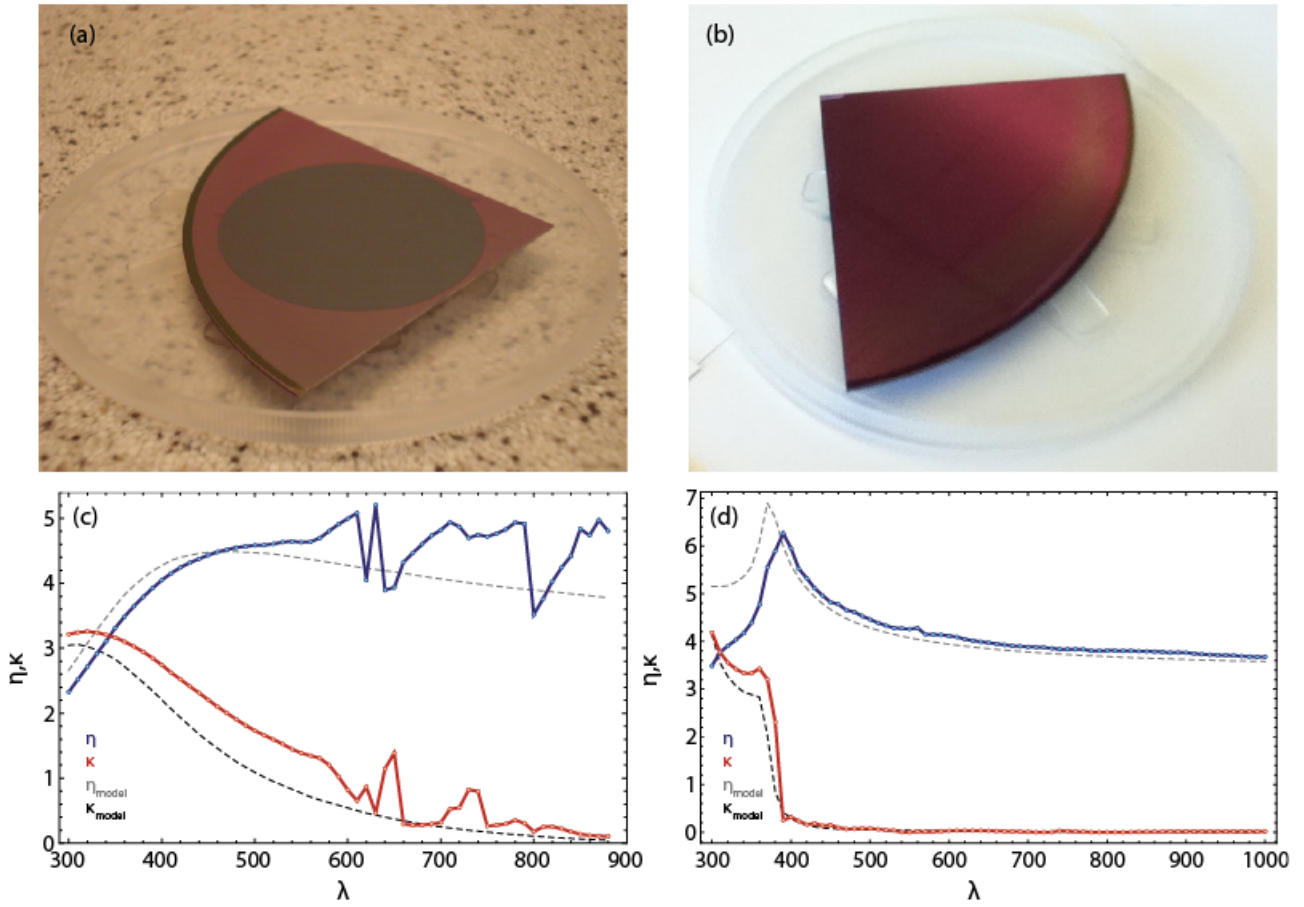
Figure 5.3: *a) Photograph of SOI wafer after ion implantation. The dark circle corresponds to the Er and O implanted area where the Si waveguide has become amorphous. The red reflection as a result of the Fabry-Perot effect is no longer observable due to the high absorption of a-Si. b) Photograph of the SOI wafer after annealing. The crystalline structure of the Si waveguide has been repaired and the red color due to the Fabry-Perrot effect in the SOI wafer is visible again. c) Optical constants of the gray area in (a), as measured with ellipsometry. The dashed lines show tabulated values for a-Si. d) Optical constants of the implanted layer after annealing, measured with ellipsometry. The optical constants match the c-Si model (dashed lines) very well, showing that annealing leads to recrystallization of the amorphous layer.*
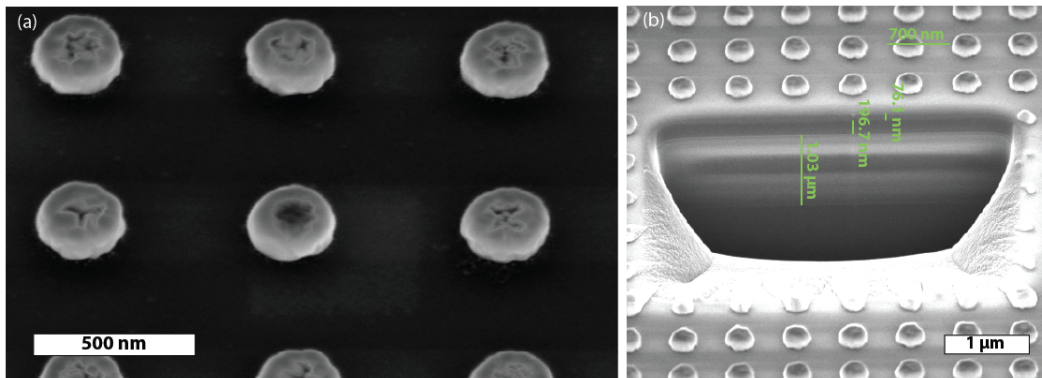

Figure 5.4: *a) SEM image showing an array of silver nanoparticles on the erbium-implanted SOI waveguide. In the particles the center part is missing, giving rise to a donut-shaped particle. b) SEM image of a cross section of the sample made with FIB milling in a 700 nm pitched field. Measurements of the layer thicknesses are shown in green.*
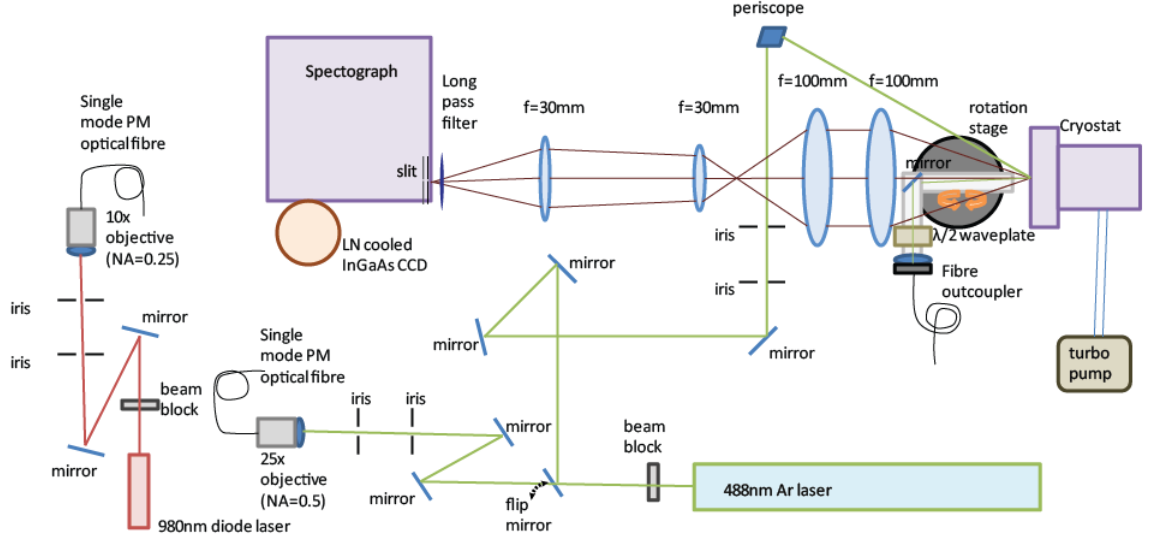
Figure 5.5: *Sketch of the PL setup.*

couple the 488 nm light into a single mode Polarization Maintaining (PM) optical fibre (OZ-optics, 3.5 μm core). For the 980 nm light a 10x objective with NA= 0.25 (Melles Griot) was used to couple the light into a single mode PM fibre (OZ-optics, 6 μm core). Either one of the fibres could be connected to a fibre outcoupler (optimized for $\lambda_0 = 980$ nm transmission), after which the light was guided through a $\lambda/2$ waveplate (optimized for either 980 nm or 488 nm) mounted in a motion controller (Newport, NSC200) to electronically regulate the polarization. The polarization angle was calibrated using a Glan-Taylor prism. To prevent large shadowing of the PL by the fibre outcoupler and motion controller, a $1/2''$ D-shaped mirror was used to reflect the light onto the sample. The angle of incidence was electronically controlled by the used of a rotation stage (Huber). The sample was mounted above the rotation axis in a cryostat using silver paste (SPI supplies) to provide good thermal conductance. Due to the window of the cryostat the angle of incidence was limited between 0 and 40 degrees. The cryostat (CTI-Cryogenics, Cryodyne M-22) was cooled with liquid helium and was pumped down using a turbopump (Oerlikon, Turbolab 80). Typical experimental conditions were $T = 14$ K at $p = 9 \times 10^{-7}$ mbar. Diffuse PL signal, radiated from the sample, was collected and transformed into a collimated beam using a large $f = 100$ mm collection lens with high NA (diameter $D = 76$ mm, NA= 0.35). A similar lens in combination with a $f = 30$ mm lens ($D = 26$ mm, NA= 0.39) was used as a telescope to reduce the radius of the beam. Finally, a $f = 30$ mm lens ($D = 51$ mm, NA= 0.64), which was f-matched with the spectrograph, was used to focus the beam down to a spot on the entrance slit of the spectrograph. All lenses were coated for optimized transmission in the IR. To prevent scattered pump light to enter the spectrograph, a long-pass filter which is transparent for $\lambda_0 > 1100$ nm was placed right in front of the entrance slit. The entrance slit was closed down to an opening of ~ 0.5 mm. A triple grating spectrograph (Acton, Spectra-Pro 2300i) was used to spectrally resolve the collected light and to project in on a CCD detector. The grating used for the PL measurements had 150 lines/mm, positioned with the center wavelength to $\lambda = 1500$ nm, resulting into a detection range 1230 nm $\leq \lambda_0 \leq$ 1770 nm. A liquid-nitrogen cooled InGaAs CCD detector was used (Princeton Instruments, Acton 7498-0001) with 1024×1 pixel array. Typical detector temperatures for experiments were $T = -75\,^\circ$ C, giving rise to low dark currents.

The PL intensity was measured at different temperatures while cooling down the sample to show the temperature dependent quenching. This measurement was performed using 488 nm light with a pump power of 23 mW on the sample under normal incidence on a non-patterned reference field, using an integration time of 4 s. Shown in Fig. 5.6 are the PL signals for $T = 293$ K (blue), $T = 200$ K (purple), $T = 100$ K (orange), and $T = 14$ K (green). A 5-value median filter is used to smoothen the data. The graph shows that lower sample temperatures reduce the PL from defect states in the Si (signal $\lambda_0 < 1300$ nm), and increases the signal from Er (peak at $\lambda_0 = 1535$ nm) due to reduced quenching. This gives rise to an increased signal-to-noise ratio.
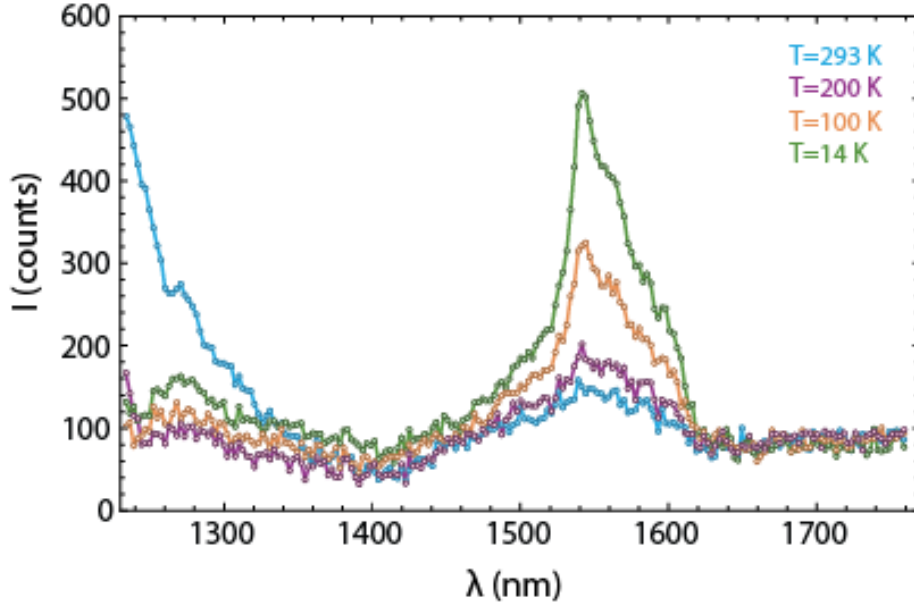
Figure 5.6: *PL spectra for a non-patterned reference fields under normal incidence for different sample temperatures: room temperature (blue), 200 K (purple), 100 K (orange), and 14 K (green). This comparison shows the benefit of cooling down the sample, namely lower PL from defect states in the Si and higher PL from Er due to the reduction of quenching. ($\lambda_{pump} = 488$ nm)*

5.3.3   Measurements and Analysis

The setup contains two pump lasers (488 nm and 980 nm). To determine the most efficient pump wavelength, two things must be considered. First, in section 2.3 the propagation length of the TE0 mode was calculated, showing a drastic increase for longer wavelengths due to the low absorption of c-Si. Therefore, the effect of light coupling to waveguide modes on the intensity enhancement inside the waveguide will be most pronounced for longer wavelengths. Second, the excitation mechanism of the erbium luminescence centers will give rise to different excitation efficiencies. As mentioned in section 5.2, light can either directly pump the Er, or pump the bandgap of Si after which the exciton can be transfered to luminescence centers. However, due to the low transfer rate of excitons from the Si to the luminescence centers, a part of the excitons will recombine radiatively both with the Si bandgap energy as well as with lower energies from the defect states in damaged Si after annealing [65]. This second mechanism will play a much more important role for $\lambda_0 = 488$ nm due to the short absorption length of this light in Si. Therefore, 488 nm pumped PL will show more signal from the Si defect states and less signatures from light coupling to waveguide modes. In Fig. 5.7, a typical PL spectrum obtained from a non-patterned reference field is shown for both pump wavelengths ($\lambda_0 = 488$ nm corresponds to red and $\lambda_0 = 980$ nm to blue). Both spectra are collected while pumping with p-polarized light, $\theta = 35°$ and sample temperature of $T = 14 \pm 1$ K. Note that the signal for the 980 nm pumped spectrum is much higher even though the pump power is much lower (7 mW instead of 21 mW for 488 nm) and the integration time is half as long (5 s instead of 10 s). Furthermore, the signal from the 980 nm pumped sample gives less noise for $\lambda_0 < 1300$ nm and shows more pronounced peaks in the right shoulder of the signal as a result of transitions between the Stark split energy levels. Based on these observations and the fact that the absorption length in Si is longer for $\lambda_0 = 980$ nm, the 980 nm laser was used for the angular dependent measurements. The measurements were performed using 7 mW of pump power, a sample temperature of 14 ± 1 K, and a 5 s integration time.

   To detect the light intensity enhancement due to coupling to waveguide modes, the PL spectrum as shown in Fig. 5.7 is measured for $0° \leq \theta \leq 40°$ with a $\Delta\theta = 0.5°$ resolution. The raw data obtained from each scan consists out of a 3-D dataset, namely the PL intensity I as a function of detection wavelength $\lambda_{detection}$ and angle of incidence θ. The detection spectra are smoothened by a 5-value median filter. An example of the resulting dataset that is used for the analysis is shown in Fig. 5.8, obtained from a field with a pitch of 700 nm and a particle diameter of 270 nm. For each angle of incidence, the peak
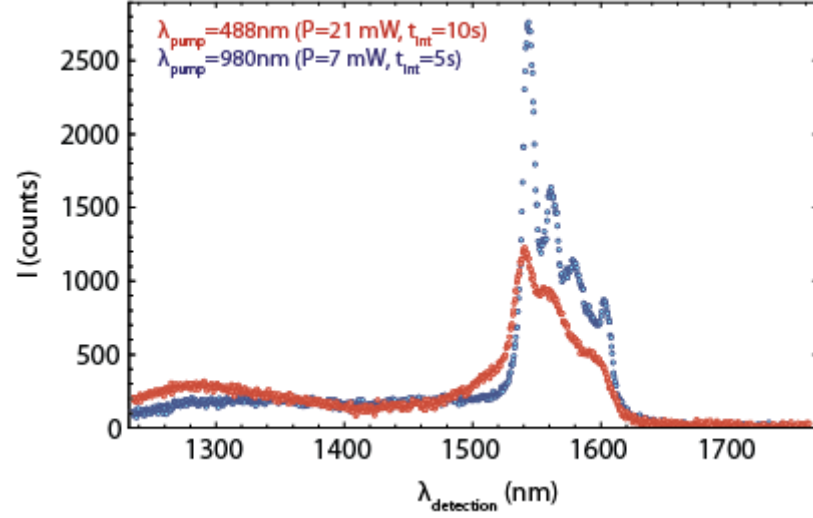
Figure 5.7: *Typical PL spectrum obtained with two different pump wavelengths ($T = 14$ K). The red curve is obtained by pumping at $\lambda_0 = 488$ nm with 21 mW and integrating the PL spectrum over 10 s. The blue curve is obtained by pumping at $\lambda_0 = 980$ nm with 7 mW and integrating the PL spectrum over 5 s. Both measurements were taken with p-polarized light and from a non-patterned reference sample with an angle of incidence of $\theta = 35°$. Note that the blue spectrum gives a higher signal with less noise for a lower pump power and integration time. Also, the small peaks in the right shoulder as a result of the Stark split energy levels of the $^4I_{13/2} \rightarrow {}^4I_{15/2}$ intra-4f transition are more clearly observable for the 980 nm pumped signal. This implies that different Er ions (different local environment) are excited for the two pump wavelengths.*
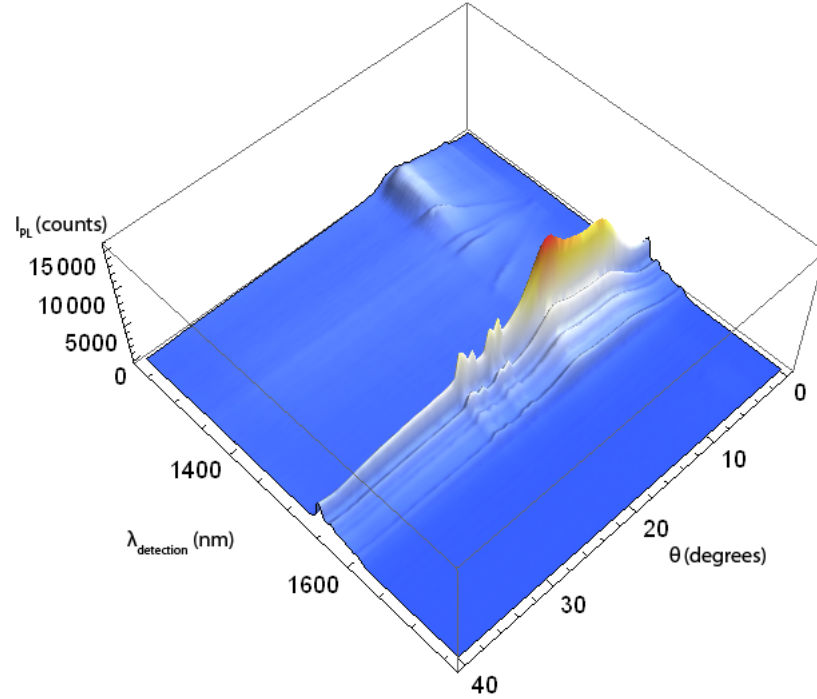

Figure 5.8: *Example of 3-D dataset after smoothening with a 5-value median filter, obtained from a measurement on a field with 700 nm pitch and 270 nm particle diameter. The maximum intensity of the erbium peak at 1.54 µm is used as the measure of PL intensity. Clear peaks can be observed for distinct angles of incidence.*

intensity of the erbium signal was used as a measure of the intensity inside the waveguide. The PL signal of the patterned fields was normalized by the PL signal of the non-patterned fields. This yields the PL

enhancement which directly measures the intensity enhancement.

5.4   Results and Discussion

Figure 5.9 shows the PL enhancement is shown as a function of angle of incidence for two polarizations: p-polarization (blue) and s-polarization (red). The results are shown for a 700 nm pitched field (a) and for a 500 nm pitched field (b). Note that the particle size of the two fields is different. In both (a) and (b) clear, distinct and sharp peaks can be observed that are assigned to the excitation of Er by well-defined waveguide modes. PL enhancement factors up to 9.7 are observed for the 700 nm pitched field. Furthermore, clear differences are observed for the two polarizations, which are ascribed to differences in mode overlap with the TM and TE waveguide modes, as discussed in section 2.6. Note that the PL enhancement for both fields and both polarization is never lower than 1, suggesting that, besides coupling to waveguide modes, the absorption inside the waveguide is also enhanced by near field coupling and the anti-reflection effect of the particle array.
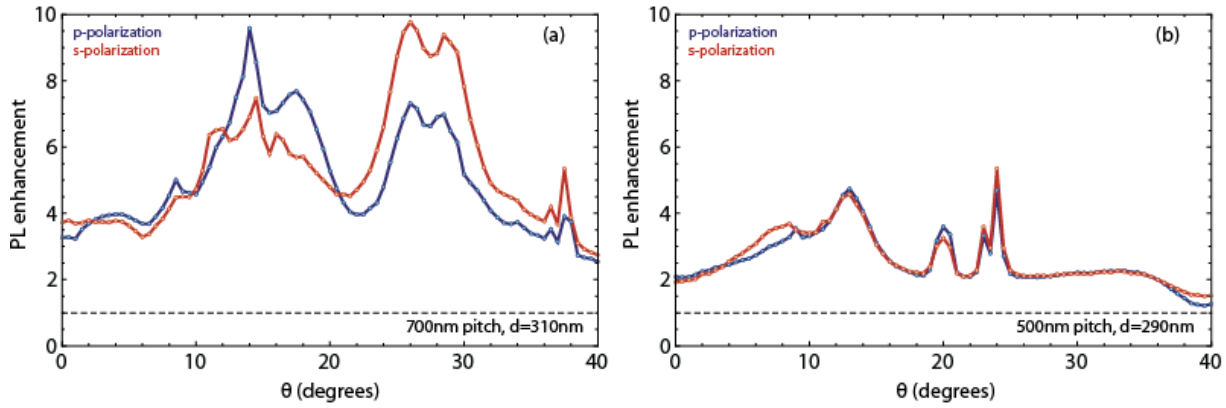

Figure 5.9: *PL enhancement as a function of angle of incidence for a 700 nm pitched field (a) and a 500 nm pitched field (b). The blue lines correspond to p-polarized light, the red lines to s-polarized light. Clear peaks are observed for both fields that are assigned to well-defined waveguide modes.*

The data clearly show the intensity enhancement due to coupling to waveguide modes. However, many details are still not fully understood and under investigation. The following discussion will focus on these details and possible explanations. Figure 5.9b shows that although peaks are present, the PL enhancement is lower for the 500 nm pitched field. This can be attributed to less efficient coupling as a result of the difference in scattering cross section, which also explains the smaller polarization dependence of the PL enhancement. Section 3.4 showed that a red shift and decrease in Q_{scat} occurs when a particle is placed in an array, as a result of inter-particle coupling. This calculation was performed with a 500 nm pitched array. A 700 nm pitched array will have less coupling and therefore a smaller red-shift and higher Q_{scat}. Therefore, the scattering cross section of the two pitched arrays at $\lambda_0 = 980$ nm is different. Comparing these results with the results of chapter 4 yields a discrepancy: total reflection measurements and simulations showed deeper reflection dips for the 500 nm pitched field, whereas the PL enhancement measurements show larger enhancement factors for the 700 nm fields.

The fact that larger and more peaks are observed in Fig. 5.9a compared to (b) could also be caused by the difference in particle size. To investigate this, the PL enhancement for similarly pitched fields (700 nm) but different particle size ($d = 270$ nm and $d = 310$ nm) is shown in Fig. 5.10a. Here, the blue and the orange line correspond to the $d = 270$ nm array (corresponding to p and s-polarization respectively), and the purple and green line to the $d = 310$ nm array. Also shown as vertical dashed black lines are the angles at which momentum matching occurs with one of the waveguide modes according to calculations. If the particle size has no significant influence on the coupling efficiency, the PL enhancement should look identical for different particle size and similarly polarized light. However, Fig. 5.10a shows that not only the peak height is different, also the peak location is different. Furthermore, the angular mismatch with the vertical lines indicates that the location of the peaks cannot be explained by momentum matching only. Additional effects seem to play a role.
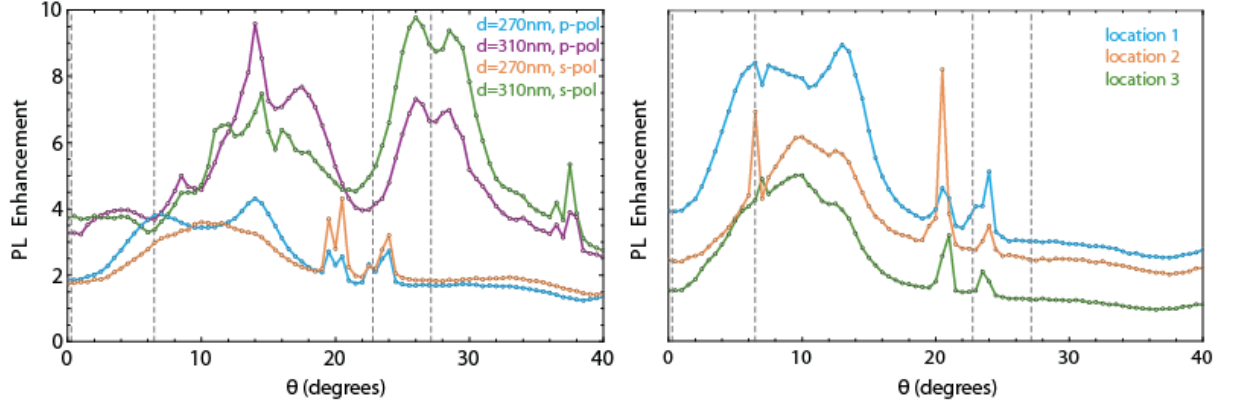
Figure 5.10: *a) PL enhancement as a function of θ for similarly pitched fields (700 nm pitch) but different particle sizes. The green and the purple curve correspond to p-polarized and s-polarized light for d = 310 nm respectively, the blue and the orange curve to p-polarized and s-polarized light for d = 270 nm respectively. The large difference between both peak location and peak height indicate that particle size does play a significant role. b) PL enhancement for three different locations on the same particle array. The peaks occur at similar angles of incidence, indicating that local damage to the particle array does not significantly alter the mechanism of light coupling to waveguide modes.*

Another possible explanation of the discrepancy in peak position in Fig. 5.10a could be damages in the particle array. The scratches and damage as shown in Fig. 4.2 may lead to variation in the interaction between the particle array and the light. To rule out this effect, the PL enhancement was measured on three different locations on the same field. Figure 5.10b shows the PL enhancement for three locations on a 700 nm pitched field with $d = 270$ nm. The different enhancement factors are a result of a small drift in the power of the pump laser. However, all three lines show peaks at the same angle of incidence, ruling out the influence of damage to the particle array as an explanation for the horizontal discrepancies in (a). Also, repeating the measurements in Fig. 5.10a yielded similar results indicating that the particle size do cause a shift in peak position.

There are 2 additional effects not yet investigated that can complicate the interpretation of the PL results. First, the presence of metal nanoparticles close to the erbium ions may enhance the local density of optical states (LDOS) of the ions, thereby enhancing their decay rate γ. If true, this would enhance the PL signal, which could also explain why the PL enhancement observed in Fig. 5.9a and b is always larger than 1. Correcting for this may lower the overall curve and might show that the PL enhancement is lower than 1 locally. This effect can be investigated by measuring the decay rate of the erbium PL. Second, the erbium ions are implanted inside the waveguide. Because this is a dielectric waveguide, the fundamental mode does not experience cut-off. For example, using the calculations in chapter 2 it can be shown that for $\lambda_0 = 1.535$ μm the TE0 mode has $\beta = 11.371\mu\mathrm{m}^{-1}$. Therefore, the erbium PL can couple to the TE0 and TM0 mode. However, the mode profile of these modes stick far outside of the waveguide, causing strong interaction with the particle array. This may alter the waveguide modes, but also allows the PL light to couple out of the waveguide under a specific angle. Using Eq. 2.10, it can be calculated that this angle is $21.9°$ for $\Lambda = 700$ nm pitched fields, and $10.7°$ for $\Lambda = 500$ nm pitched fields. Since the collection angle of the detection branch is $\sim 20°$ for this setup, such light is collected for only one of the pitches. To check whether this effect has a large influence on the detected signal, the PL signal as a function of detection angle will be measured.

To further explore the angular dependence of the momentum matching, as well as to check the correspondence with the PL measurements, the specular reflection was also measured as a function of angle of incidence. A simple setup was used, as shown in Fig. 5.11a. A 980 nm diode laser (Witec) was used in combination with a single mode PM fibre (OZ-optics, 6 μm core) to illuminate the sample. Illumination powers (on sample) were ~ 1 mW for p-polarization and ~ 300 μW for s-polarization. The polarization was controlled by a polarizer mounted in a motion controller (Newport, NSC200). The sample stage as well as the power meter (Thorlabs, PM300) were mounted on a double rotation stage (Huber) to measure the specular reflection for all θ. The measurements were performed with a $1°$ resolution. To check the reliability of the measurement procedure, the specular reflection of a non-patterned reference field was measured and compared to Fresnel calculations. The results are shown in

Fig. 5.11b. The qualitative agreement is good, but small deviations can be observed, especially for high angles of incidence. As expected from theory, the dip in reflection as a result of the Brewster angle is clearly observed for the p-polarized light.
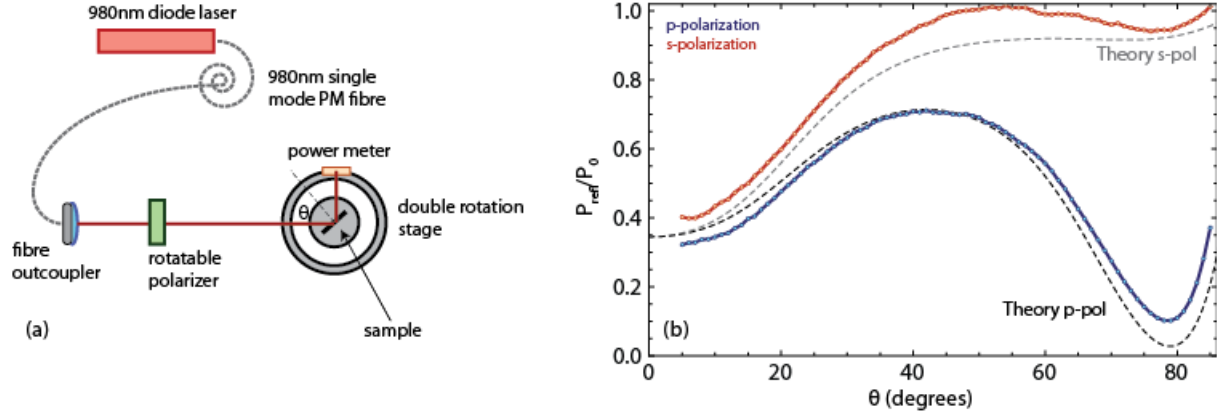

Figure 5.11: *a) Sketch of the setup used to measure angular resolved specular reflection. b) Measured specular reflection as a function of angle of incidence of a non-patterned reference field for s-polarization (red) and p-polarization (blue). Also shown in black and gray are the reflections for p and s-polarization according to Fresnel calculations.*

The same measurement procedure is used to measure the specular reflection of patterned fields. Figure 5.12 shows the comparison between the PL enhancement and the specular reflection as a function of θ for the 700 nm pitched field ((a) and (c)) and the 500 nm pitched field ((b) and (d)). Also shown as gray dashed lines are the angles at which momentum matching occurs with one of the waveguide modes. When light couples to a waveguide mode, the PL enhancement is expected to show a peak whereas the specular reflection is expected to show a dip. From Fig. 5.12 we can observe that most of the clear
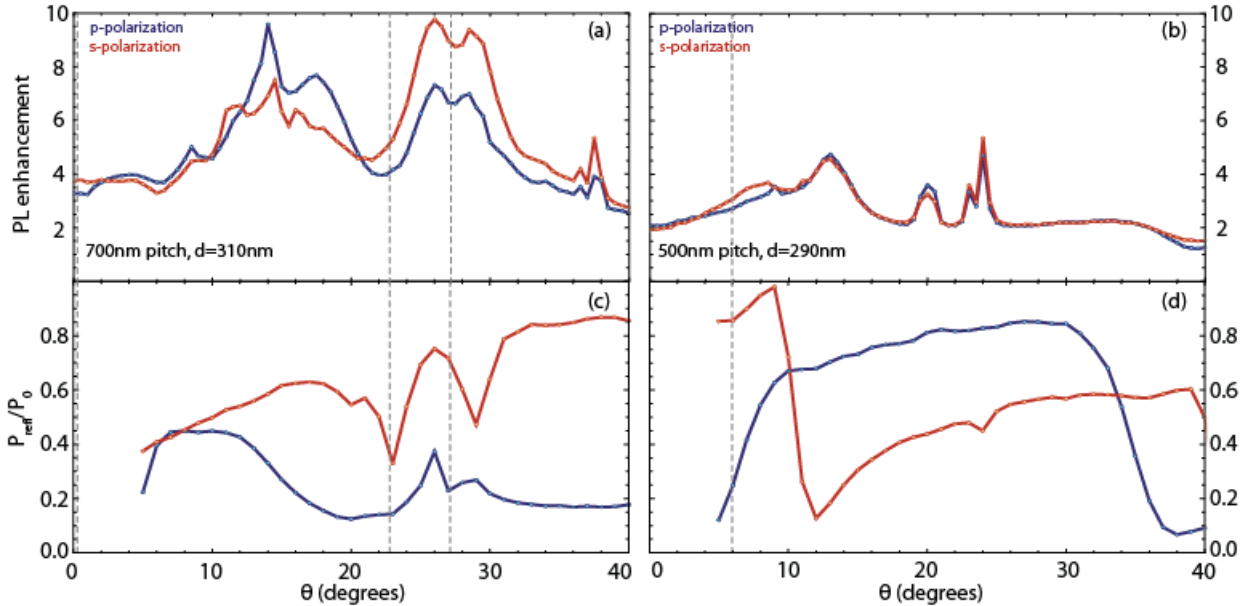

Figure 5.12: *Comparison between PL enhancement (a) and b)) and specular reflection (c) and d)) as a function of angle of incidence, for a 700 nm pitched field (a) and c)) and a 500 nm pitched field (b) and d)). The vertical gray dashed lines correspond to the angles at which momentum matching with one of the modes is fulfilled.*

peaks in the PL enhancement are accompanied with a observable dip in the reflection signal. This is most pronounced for the 700 nm pitched field where the dips also occur close to the calculated angles. However, the PL enhancement shows additional peaks that are not observed as dips in the reflection

signal. Furthermore, the peaks observed in the PL enhancement for the 500 nm pitched field do not match with the calculations. The fact that the dip at $24\,^\circ$ in Fig. 5.12d is so small indicates that the specular reflection is not very sensitive to light coupling to waveguide modes. This may explain why other even smaller peaks in the PL enhancement do not give a observable dip in the reflection signal. The contrast with the clear observation of mode-coupling dips in the total reflection measurements of chapter 4 suggest that it is mostly the power scattered in the non-zero diffraction orders - which are not collected in specular reflection measurements, but are in integrating sphere measurements - that contributes to coupling to waveguide modes. Finally, the discrepancies with the calculations are more pronounced in the PL enhancement than in the specular reflection signal, suggesting that several other effects that are not yet considered play a role in the PL enhancement.

5.5 Conclusions

After observing light coupling to waveguide modes in chapter 4, a new method is used to probe the intensity enhancement inside the waveguide. By measuring the PL intensity of optically active Er ions inside the waveguide as a function of angle of incidence, clear peaks were observed that are assigned to pump-light coupling to well-defined waveguide modes. Angle-resolved specular reflection measurements are used to further investigate the angular dependence of momentum matching and to compare with the PL measurements. Good correspondence is observed between dips in reflection and the most pronounced peaks in the PL enhancement, but smaller PL peaks are not accompanied by dips in the reflection signal. This suggests that it is mostly the power scattered in the non-specular diffraction orders that attributes to coupling to waveguide modes. Furthermore, the discrepancies between the angles of the peaks in the PL enhancement and the calculated angles at which momentum matching is fulfilled, indicate that more complex effects are involved that are not yet understood. In future research we will focus on resolving these effects and applying this method to further optimize scattering structures with respect to efficient light trapping in waveguide modes.

Chapter 6

Supernormal Transmission in Resonant Transparent Conducting Electrode Networks

6.1 Introduction

In the previous chapters we have shown that silver nanoparticle arrays allow light to couple to waveguide modes in the substrate. Besides this, silver can also be used for the electrical contacts on top of solar cells due to its low resistance. It is therefore interesting to study whether the electrodes can be combined with the light trapping scheme in one fabrication step. To explore this, we design and fabricate a silver metal nanowire network which is both transparent and conducting. Transparent conducting electrodes are essential for the performance of optoelectronic devices. a-Si and organic solar cells, LEDs and television screens are all dependent on the transparent and conducting properties of such materials. Indium-Tin-Oxides (ITO) are commercially used for such applications. However, ITO has several important drawbacks: (1) the cost of sputtered ITO is high [66, 67], (2) ITO layers are brittle [66–68], (3) the sputtering process causes damage to organic layers, thereby reducing device performance [66], (4) it has poor chemical compatibility [67], (5) ITO strongly absorbs in the blue spectral region [23], and (6) in case of solar cells, the band structure of ITO hinders efficient photocurrent generation in the UV/blue spectral range [68]. These problems motivate the search for new transparent conducting electrodes that overcome these problems. In fact, metallic grids in combination with ITO [69], solution-processed random metal nanowire meshes [70, 71], one dimensional nano-imprinted metal electrodes [68, 72], and other designs have been investigated as a possible replacement for ITO. Each design represents a trade-off between optical transmittance and electrical conduction. Thicker and more dense layers provide better electrical conduction but reduce the transmission and vice versa. Also the compatibility with optoelectronic device fabrication techniques limits the applicability of many of these designs.

Recently, a detailed analysis of the physics of the transmission of light through 1-D and 2-D metal nanowire networks has shown how a combination of guided optical modes in MIM waveguides (formed by the combined nanowires) and SPPs on the nanowires determine the optimal design of such networks [66]. Thin, high aspect ratio wires are evaluated to have optimum transmission without losing electrical conductance. The 1-D design has already been realized experimentally [67], yielding performances comparable to ITO. This structure, however is only effective for one polarization. The two dimensional configuration on the other hand, has so far not yet been realized. Here, we design and fabricate a 2-D network of narrow (tens of nanometers) nanowires with low aspect ratio to explore the performance of such nanowire networks as transparent conducting electrodes. By changing the wire diameter, aspect ratio and network pitch, both transmittance and electrical condictivity can be tuned and optimized. Furthermore, the two dimensional character of the network allows light coupling to waveguide modes for both polarizations. This design can therefore be optimized to combine the electrode functionality with light trapping schemes.

6.2 Calculations and simulations

To characterize the electrical properties of the networks, analytical calculations are used. As a first approximation we consider the 2-D wire mesh as a 2-D network of resistors with fixed resistance R. The resistance of such a network of nanowires is then calculated by solving Kirhoff's rules for each node and all loops in the network. For large square networks with N resistors in both dimension, this calculation can easily be written in matrix form. First, the effective resistance R_{eff} (in units of R) between two nodes on the side of the network has been calculated. The inset of Fig. 6.1a shows the configuration where the resistance between the two blue dots (separated by N resistors in the horizontal direction) is calculated, as well as the resistance along the diagonal (purple dots) of a $N \times N$ sized network. Fig. 6.1a shows R_{eff} as a function of network size N for both configurations. An increasing resistance is observed for increasing size, as a result of the increasing number of resistors between the two nodes. The diagonal has a larger resistance as a result of the larger path length with respect to the horizontal case. However, a converging behavior is observed for large networks as a result of the many parallel paths that become available to the current.
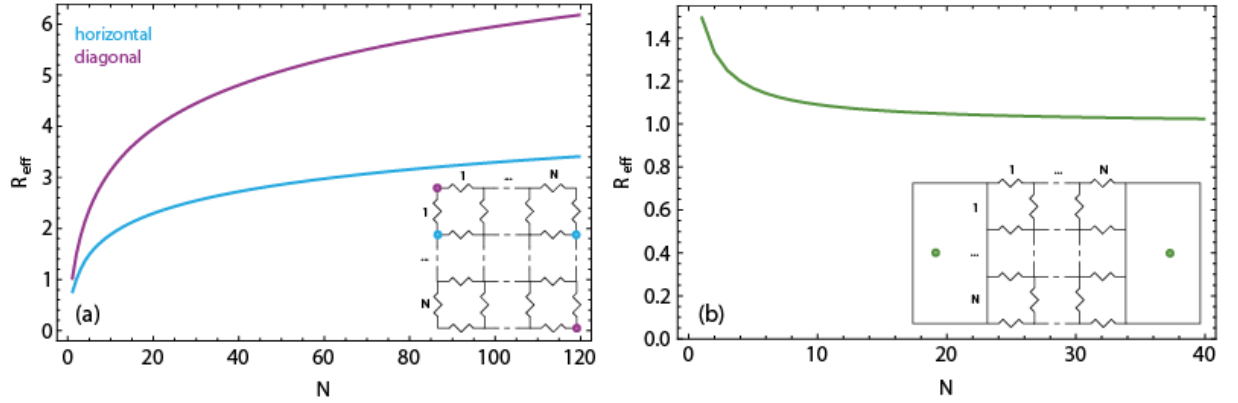

Figure 6.1: *The effective resistance R_{eff} in units of R as a function of network size N between two points in the network.* **a)** *shows the resistance between two horizontal points (blue) and two points along the diagonal of a $N \times N$ network (purple). The inset shows a sketch of the point probe position. An increasing effective resistance is observed that converges for large networks.* **b)** *shows the resistance of a network with large pads on either side, in which the resistance is assumed to be negligible (see inset). As a result, the current will only flow in the horizontal direction. A decreasing effective resistance is observed that converges to 1 for large network sizes.*

Based on these calculations, larger networks are determined to have higher resistance. However, in the experiments, the side of each network is in contact with a large pad, providing a low resistance path in the vertical direction. Assuming zero resistance in the pads, the resistance is calculated between the two pads, as indicated by the green dots in the inset of Fig. 6.1b. The effect is that no current flows through the vertically oriented resistors, such that the effective resistance of a $N \times N$ network is just the effective resistance of $N + 1$ parallel wires with a resistance of NR: $R_{eff} = \frac{N}{N+1} R$. The result is shown in Fig. 6.1b where R_{eff} (in units of R) is again shown as a function of network size N. The effective resistance decreases for larger network and converges to 1.

These calculations show the trend that can be expected in measurements, but are based on the assumption that all wires have exactly the same resistance, that there are no defects in the wires and that the pad-network contact is perfect over the entire length of the network.

To get insight in the optical properties of the network, numerical simulations are performed. FDTD simulations have been used to calculate the transmission through an infinite metal nanowire network. The simulation setup is shown in the inset of Fig. 6.2, where one unit cell of the simulation is shown. Periodic boundary conditions using a 500 nm pitch, were used to simulate an infinite network. A broad band (300 nm $\leq \lambda_0 \leq$ 1000 nm) plane wave at normal incidence is used as a source, and a transmission monitor (red dotted line) at the surface measures the power transmitted into the substrate. The substrate is assumed to have $n = 1.5$ and to be non-absorbing. The optical constants for silver are obtained from a Drude-Lorentz fit to the data from Palik [49]. The nanowires are assumed to have a square cross section, with a wire width and height ranging from 30 nm to 70 nm, and spaced by a pitch of 500 nm.
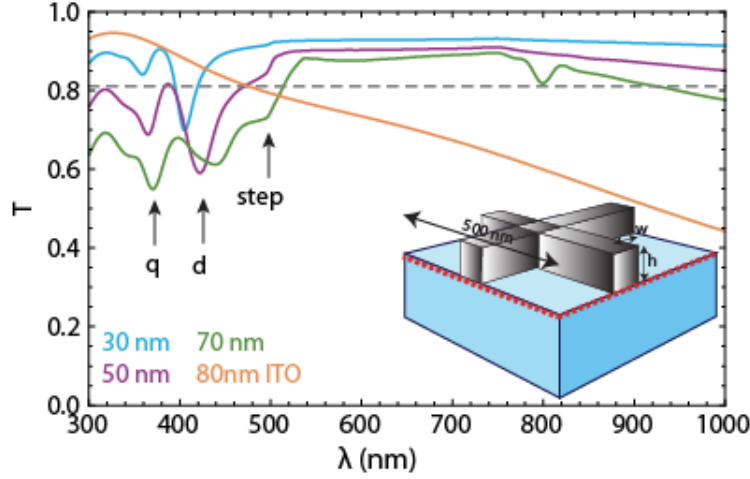
Figure 6.2: *Calculated transmission for networks with a wire width and height of 30 nm (blue), 50 nm (purple) and 70 nm (green). Also shown is the fraction of uncovered surface area (dashed line, based on 50 nm wire geometry) and the transmittance through a 80 nm ITO layer on a glass substrate (orange, based on Fresnel calculations). A constant supernormal transmission (T >surface area) is observed for the networks which is higher than for the ITO layer for the 500−1000 nm spectral region, with a sharp dip in transmission at the locations of the dipole (d) and quadrupole (q) resonance. A red-shift is observed for the dipole resonance for increasing wire dimensions. The ITO layer shows a decreasing transmittance for larger wavelengths. The simulation setup with the transmission monitor (red dotted line) is shown as an inset.*

Figure 6.2 shows the simulated transmission as a function of wavelength for $w = h = 30$ nm (blue), 50 nm (purple), and 70 nm (green). Also shown is the fraction of uncovered surface (dashed line, based on 50 nm wire geometry) and the transmittance through a 80 nm ITO layer on a glass substrate (orange). The transmittance through the ITO is determined by Fresnel calculations, with the optical constant for ITO obtained from ref. [73]. A 80 nm layer is commercially used as a good conducting and effective anti-reflection (AR) coating on a-Si solar cells. The ITO shows decreasing transmittance for longer wavelength as a result of reflection and absorption (above $\lambda_0 = 800$ nm), and a peak at $\lambda_0 = 325$ nm as a result of the AR effect. Although the transmittance through ITO on glass is poor, the refractive index of ITO provides very efficient impedance matching when placed on a-Si. For the metal wire networks, the arrows depict the locations of the dipole resonance (d) which red-shifts for larger wire dimensions, and the quadrupole resonance (q) which shows only a small red-shift for larger wire dimensions. It can also be observed that the feature in the transmittance at the dipole resonance is less pronounced for larger wire dimensions. Although the simulated wires show a strong reduction in transmission for the blue spectral range, this graph clearly shows that by changing the wire dimensions, the dipole resonance can be shifted outside the spectral region of interest. Furthermore, above resonance a supernormal (T > uncovered area) and flat transmission profile larger than 85 % is observed, which decreases for larger wire dimensions due to the increasing shadowing effect. This transmission is higher than for the 80 nm ITO layer for the 500−1000 spectral region. The tranmittance through the network slowly decreases for $\lambda_0 > 800$ nm, but this is not attributed to the cut-off of fundamental MIM waveguide modes between the wires as in ref. [66]. In contrast to ref. [66], the low aspect ratio of our wires construct a poor MIM waveguide. Finally, a step-like increase in transmission is observed at the same wavelength as the network pitch (500 nm, indicated by an arrow in Fig. 6.2), which is more pronounced for larger wire dimensions. This feature is caused by the resonant excitation of a surface wave (SPP) on the network (Wood's anomaly) and is also observed in similar simulations in ref. [67].

6.3   Methods

6.3.1   Sample Fabrication

A SiO_2 substrate is used to allow both high transmission for optical measurements and electrical insulation for electrical measurements. The silver network was fabricated using Electron Beam Lithography (EBL).

Before further processing, the glass slides were cleaned using a basic cleaning recipe based on H_2O_2 and NH_4OH. Before depositing resist, a thin film of HMDS primer was spin coated at 4000 rpm (30 s) to improve the adhesion to the glass substrate. After baking at 150 °C for 1 min, the resist (5:2 ZEP520A:Anisole) was spin coated with 2000 rpm (45 s) to obtain a 150 nm thick layer. The resist was dried by baking at 150 ° for 5 min. A small droplet of Au colloids (250 nm diameter) suspended in deionized H_2O was deposited to allow efficient focusing of the electron beam. Finally, a layer of conducting polymer (Espacer) was spin coated (3000 rpm, 45 s) to prevent the glass substrate from charging.

Networks of nanowires with 500 nm pitch were written with a 20 kV electron beam (current ~ 0.16 nA, dwell time ~ 0.6 μs, step size ~ 10 nm) using single pixel lines. The dose ranged from $320 - 410$ $\mu C/cm$ to vary the nanowire diameter. After development, silver was deposited using thermal evaporation. A 50 ± 5 nm layer was deposited at an initial pressure of $p \sim 5 \times 10^{-7}$ mbar and with deposition rate 4 $\mathring{A}/s$. Lift off was performed by soaking in anisole (phenoxymethane) for $3 - 5$ hours, followed by 3 repetitions of subsequent steps of 1 minute sonication in anisole, rinsing with 2-isopropanol (IPA) and optical microscopy imaging. The final sample contained 4 different network sizes (25 μm, 50 μm, 75 μm and 100 μm in both dimensions) and 4 different doses. The entire matrix (16 networks) was repeated multiple times on the sample to obtain statistics. The pads on the sides of the network were written using area exposure (350 $\mu C/cm^2$, same beam current, step size and dwell time as network) and were designed to overlap 500 nm with the network to provide good electrical contact. Figure 6.3 shows three
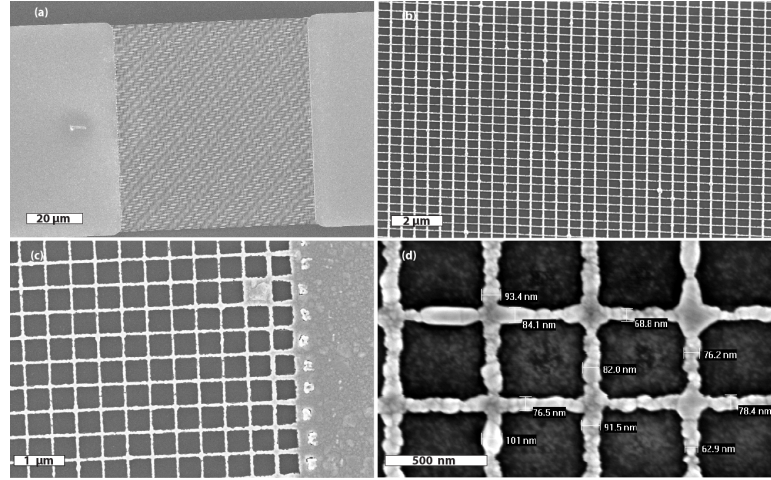

Figure 6.3: *SEM images of the network, with four different magnifications. (a) shows the geometry of the pads and the network, (b) shows how uniform the network is, (c) shows how the pads are connected to the network, and (d) shows the wire quality and measurements of the wire thickness.*

SEM images of the network. Figure (a) shows a 75×75 μm network with 75×50 μm silver pads on the side, clearly showing how uniform the network is and how the pads are located at the side of the network. Figure (b) uses a larger magnification to show that few defects are present in the network, (c) shows how well the pads are connected to the network, and (d) shows both how good the wire quality is and how the silver grains cause irregularities in the wire thickness. Using SEM, the wire thickness was measured to be $60 - 100$ nm (see Fig. c), depending on the electron beam dose. Using a black and white filter on SEM images, the surface coverage by the silver was determined to be 25 ± 1 %.

6.3.2   Setup and Measurements

Optical transmission measurements were performed using a confocal microscope (Witec, α). A sketch of the setup is shown in Fig. 6.4a. A white light source (ANDO, AQ-4303B) illuminates the sample with unpolarized light through a 25x objective (Nikon, NA=0.5). The transmitted light is collected using a 50x high NA objective (Melles Griot, NA=0.7), coupled into a fibre and fed into a spectrometer, consisting out of a spectrograph (Acton, SpectraPro 300i) and a Si CCD array (Princeton Instruments). The spectral range detected in the CCD was 420 nm $\leq \lambda_0 \leq$ 975 nm. The transmitted spectrum was normalized by the transmission through the bare glass. The transmission of the 50 μm, 75 μm and 100 μm network and the glass reference were measured on 6 different locations for all doses and averaged to
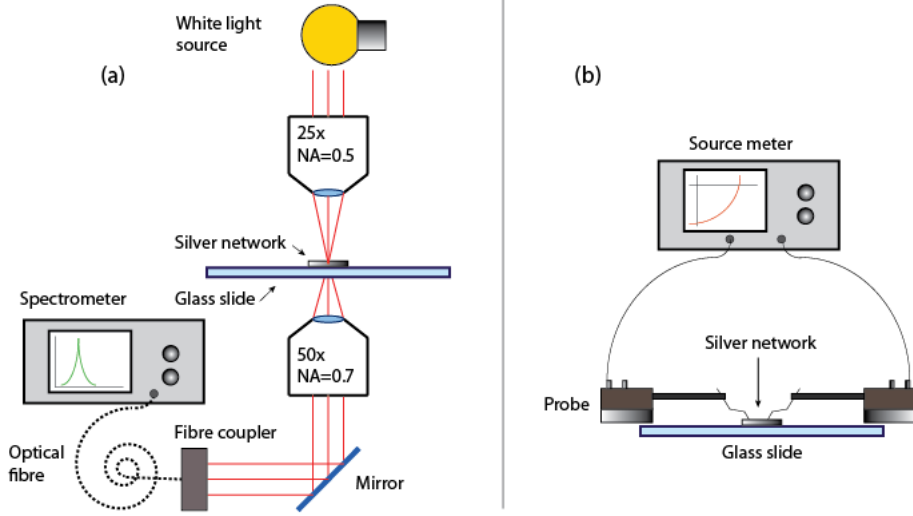
obtain a reproducible transmission spectrum.

Figure 6.4: *Sketch of the setup used for the optical transmission measurements **(a)** and for the electrical resistance measurements **(b)***

The electrical resistance of the networks was measured with a 2 probe experiment. The setup is shown in Fig. 6.4b. Electrical probes (Süss MicroTec, PH100) were brought in contact with the pads and connected to a source meter (Agilent, U2722A). *I-V*-curves were measured by ramping the current through the network from 0 to 1 mA and measuring the voltage over the network. A linear fit to the data was used to determine the resistance of each network. Measurements showed that different doses (small variations in the wire width) had no significant influence on the resistance. For electrical measurements, the 50 μm and 75 μm network the fields written with a dose of 350 μC/cm were used, for the 100 μm network the dose of 320 μC/cm was used.

6.4   Results and Discussion

The quality of a transparent conducting electrode is determined by two parameters: optical transmittance and electrical resistivity. Figure 6.5a shows the transmittance spectra of a 75 μm network for different e-beam doses. The different doses correspond to different wire widths, as indicated by the sketch in the inset. After normalization to the transmittance of bare glass, all doses show a broadband transmission higher than 0.8. The transmission averaged over the $400-975$ spectral range is 85 % for all doses except for the lowest dose which has a slightly higher transmission (87 %) as expected due to less shadowing. When weighted for the AM1.5 spectrum the average transmission becomes 86.6 % for dose 320 μC/cm, 84.6 % for dose 350 μC/cm, 84.6 % for dose 380 μC/cm, and 84.3 % for dose 410 μC/cm. This is better than the average transmittance of 82 % of a glass slide covered with ITO [67]. Furthermore, the transmission shown in Fig. 6.5a is almost constant over the entire spectral range, in contrast with the transmittance of ITO which peaks at 600 nm but drops to 65 % at 400 nm [67], due to the strong absorption in ITO in the blue [23]. Taking into account the 25 % surface coverage, supernormal transmission is observed. This is shown in the inset of (a), where the transmission through the network written with dose 350 μC/cm is normalized to the uncovered area. The average normalized transmission is 113 %, indicating that the fraction of light that is transmitted is larger than the fraction of area that is not covered by the network. The transverse resonance of the individual nanowires is not observed in the transmission spectra. This can either be caused by the fact that the resonance is outside the visible part of the spectrum due to the larger width of the wires compared to simulations, or by the fact that the wires are not perfectly uniform (see Fig. 6.3d), causing broadening of the resonance.

Figure 6.5b shows the transmission for different network sizes with the same dose (350 μC/cm), as indicated by the sketch in the inset. The transmission is shown for a 50 μm (green), 75 μm (orange) and 100 μm (blue) network. As expected, the transmission spectrum is similar for all network sizes, with an average transmission (weighted for AM1.5 spectrum, in brackets) of 84 % (83.6 %) for the 100 μm
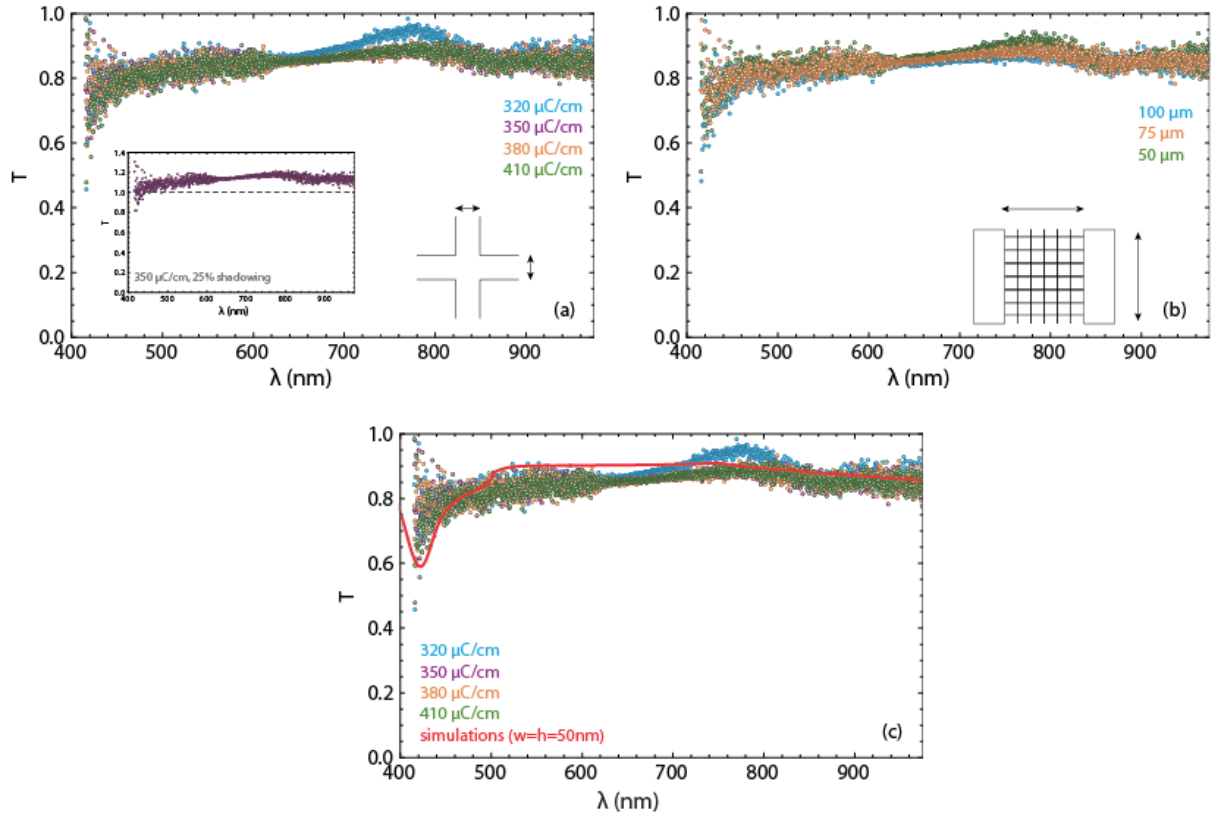
Figure 6.5: *a)* *Transmittance of a 75 μm network, written with different e-beam doses (different colors). A flat broadband high transmission is observed for all doses, with an average of at least 85 %. The different doses result into slightly different wire width, as shown by the sketch in the inset. The small changes in wire width have no significant influence on the transmission. The left inset shows the transmittance of one of the samples after correcting for the 75 % surface coverage of the silver. Supernormal transmission (average 113 %) is observed.* *b)* *Transmittance of different sized networks written with a dose of 350 μC/cm. The spectra overlap, indicating that the network size has no influence on the transmission. The inset shows the network geometry, for which the size is varied.* *c)* *Transmittance of a 75 μm network for different doses (as in (a)), overlaid with the simulated transmittance of a network with 50 nm wire diameter (as in 6.2). The data shows good correspondence with the simulation.*

network, 85 % (84.6 %) for the 75 μm network, and 86 % (85.7 %) for the 50 μm network. This indicates that the networks are uniform for all network sizes. Figure 6.5c shows the good correspondence of the measured data to the simulated transmission ($w = d = 50$ nm), showing a constant transmission > 80 % for wavelengths larger than 500 nm. The data also show a decreasing trend near the dipole resonance at $\lambda_0 = 410$ nm, which is located on the edge of the detected wavelength range.

The electrical resistance is measured for the same network sizes. Figure 6.6 shows the *I-V* curves for the 50 μm network (purple), the 75 μm network (green), and 100 μm network (blue). The resistance, as obtained from a linear fit to the data, is also shown for each network size and it ranges from 19 Ω to 75 Ω. It is clearly visible that larger network sizes result into lower resistivity. This can be attributed to two effects. First, as found in the calculations, larger networks provide more parallel paths for the current to flow, and second, defects in the network become less relevant as they can more easily be circumvented through one of the many paths available. This also shows why, besides more efficient charge carrier collection in a-Si solar cells, the vertical nanowires are relevant in experiments, even though no current flows through them in calculations.

The decreasing trend corresponds qualitatively with the calculations shown in Fig. 6.1b. However, the calculations show that for $N = 40$, corresponding to a 20 μm networks, the effective resistivity should be almost similar to the resistance of 1 nanowire. Using the resistivity of bulk silver $\rho = 1.58 \times 10^{-8}$ Ωm [74], a wire width of 60 nm and height of 50 nm, the resistance of a 500 nm long wire is calculated to be 2.65 Ω. The deviation, roughly a factor 10, is attributed to fabrication effects such as changing wire
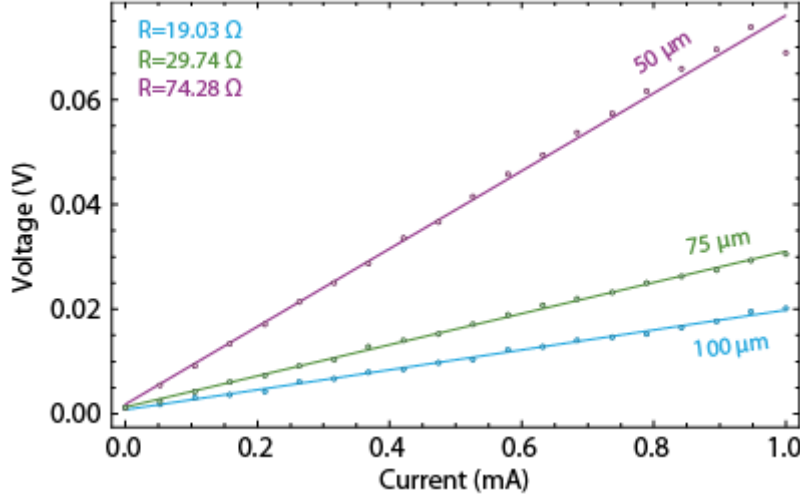
Figure 6.6: *I-V curves for the different network sizes: 50 µm (purple), 75 µm (green), and 100 µm (blue). The resistance, as obtained from a linear fit to the data is also shown for each network. This clearly shows that larger networks give rise to lower resistance.*

diameter, silver grain boundaries, and defects in the network. In ref. [67], the resistance of a 3×4 mm ITO layer on glass is measured to be 7 Ω. Given the fact that the resistivity of a 100×100 µm networks is already as low as 19 Ω and that larger networks give lower resistance, our metal nanowire network is likely to have lower resistance on such large areas.

Future experiments will focus on transmission measurements with an integrating sphere and electrical measurements with a four-point-probe setup. The transmission measurements are strongly dependent on the NA of the collection objective. In fact, light scattered at an angle larger than the collection angle of the objective is not collected. Also, the periodic nature of the network allows light to couple to waveguide modes in the glass substrate. This light is also not collected. The true transmittedance in the wafer may thus be even higher than measured. Samples with a large area network (4×4 mm) are fabricated to do transmission measurements with an integrating sphere. Although light coupled to waveguide modes will still not be collected, the collection of all NA will further improve the measured transmission through the network. Furthermore, the resistivity of conducting films, such as metal films and ITO layers, are generally expressed in terms of sheet resistance (Ω/sq.). In future experiments samples with larger pads will be fabricated to allow the location of 2 probes, such that four-point-probe measurements can be performed to measure the sheet resistance.

6.5 Conclusions

We designed and fabricated a two-dimensional metal nanowire network as an effective transparent conductive electrode to replace ITO. Using FDTD simulations we show that by varying the wire diameter, the dip in transmission as a result of the dipole resonance can be shifted outside the visible spectrum. Classical calculations based on Kirchoff's laws showed how increasing the network size would ultimately reduce the effective resistance of the network to the resistivity of one single nanowire. Using EBL, silver nanowire networks were fabricated with varying network size and wire diameter, with an average area coverage of 25 ± 1 %. Optical transmission measurements showed that the transmittance of all network sizes and wire diameters exceeded the transmittance of commercially used ITO layers. Supernormal transmission is observed when the surface coverage of the network is taken into account. Furthermore, we show that larger network sizes result into lower resistance, in agreement with calculations. Also, the trend of decreasing resistance for increasing network size suggests that for large areas, our network design will have less resistance than an ITO layer. Furthermore, the small variations in the diameter of the fabricated wires were found to have a negligible influence on both the transmission and the resistance of the network. Future experiments will use integrating sphere measurements for more accurate transmission measurements, as well as four-point-probe electrical measurements to measure the sheet resistance of the network. This will allow more detailed comparison with the transmission and sheet-resistance of

commercially used ITO samples.

Chapter 7

Conclusions and Outlook

A SOI wafer is used as a model system to study the interaction between two-dimensional arrays of plamsonic nanoparticles and waveguide modes in the substrate. The 160 nm thin top Si layer of the SOI wafer functions as an isolated waveguide that supports a discrete set of modes. Using full EM theory, we identified and calculated the dispersion curve of all waveguide modes. Momentum matching between the incoming light and the in-plane wavevector of these waveguide modes is used to describe the mode coupling mechanism. Finite-Difference-Time-Domain simulations were used to study the influence of Fabry-Perot resonances and inter-particle coupling on the reflectivity. The results show that mode coupling results into a drastic increase in the absorption inside the waveguide. We used a novel inexpensive soft-imprint method to fabricate large two-dimensional silver nanoparticle arrays with different particle diameter and array pitch on SOI wafers, to experimentally study mode coupling. Spectrally resolved total reflection measurements were performed that showed that light coupling to waveguide modes gives rise to sharp dips in the reflectivity, in full agreement with calculations and simulations.

We presented a new method to directly measure the intensity enhancement inside semiconductor layers. Optically active Er ions were implanted inside the waveguide. The photoluminesce of Er^{3+} at 1.54 μm, where Si is transparent, is used as a measure of the Er excitation rate at 980 nm. In this way, the enhancement of the PL signal is a direct optical probe of the intensity enhancement inside the waveguide. This method can therefore be used to study light trapping without the need to take into account the charge collection properties of e.g. a photodiode.

We use this method to prove that light is absorbed inside the waveguide. By changing the angle of incidence of the pump beam, angle-resolved measurements of the PL enhancement are performed. Clear peaks are observed that correspond to well-defined waveguide modes. Intensity enhancement factors up to 9.4 are measured as a result of mode coupling. Also, angle-resolved specular reflection measurements show dips in reflectivity for the same angles of incidence. However, discrepancies between the angles of the peaks in the PL enhancement and the calculated angles at which momentum matching is fulfilled, indicate that more complex effects are involved that are not yet understood. Further work is needed to investigate this in detail. This method is a very promising tool to investigate and optimize light trapping in thin-film solar cells with patterned front and back contacts for a broad variety of semiconductor materials.

Future research will focus on Er lifetime measurements and angle-resolved detection of the PL signal to study the problems discussed above. Also, further development of the PL setup as a tool to investgate light trapping will allow for more controlled measurements. In fact, by including a telescope and a low intensity allignment laser in the setup, good alignment can be guaranteed.

Motivated by the ability to efficiently trap light with periodic metal structures and the low electrical conductivity of silver, resonant transpartent conducting networks are designed to combine light trapping schemes and electrical contacts on solar cells. Using Electron-Beam-Lithography, silver nanowire meshes are fabricated that are optimized for high transmission without losing lateral condictivity. Such network electrodes can function as a replacement for ITO on a-Si solar cells, LEDs and other optoelectronic devices, thereby solving many of the problems that are related to the use of ITO. Using optical transmission measurements, we show that the networks exhibit supernormal transmittance which is higher than the transmittance of commercially used ITO. Furthermore, electrical I-V measurements show a decreasing resistance for increasing network sizes that has the potential to outperform the conductivity of ITO as well. Future reseach will focus on transmission measurements with an integrating sphere and four-point-

probe measurements to allow for more detailed comparison.

Altogether, this work shows that efficient light trapping can be realized by coupling to waveguide modes in thin semiconductor layers. By probing the intensity enhancement of Er-doped layers in structures with different particle geometries the particle arrays can be further optimized. The experiments so far focussed on light trapping by two-dimensional regular arrays. By randomizing the particle location and size, the spatial frequencies of the particle array can be tuned to have better and more broad band overlap with the in-plane wave vectors of the waveguide modes. In future research, the erbium PL mode coupling probe technique will be used to investigate the mode coupling efficiency of engineered random particle arrays.

Part of this work has been published in a review article on plasmonic light trapping in thin films solar cells: P. Spinelli, V. Ferry, J. van de Groep, C. van Lare, M. Verschuuren, R. Schropp, H. Atwater, and A. Polman, *Plasmonic light trapping in thin-film Si solar cells*, Submitted to Journal of Optics (2011).

Bibliography

[1] P. F. et al., *Techology Roadmap Solar Photovoltaic energy*, Technical report, International Energy Agency, 2010.

[2] R. Ross, *Some Thermodynamics of Photochemical Systems*, Journal of Chemical Physics **46**, 4590 (1967).

[3] T. Tiedje, E. Yablonovitch, G. Cody, and B. Brooks, *Limiting Efficiency of Solicon Solar Cells*, IEEE Transactions on Electron Devices **31**, 711 (1984).

[4] T. Markvart, *Thermodynamics of losses in photovoltaic conversion*, Applied Physics Letters **91**, 064102 (2007).

[5] P. Würfel and W. Ruppel, *Upper Limit of Thermophotovoltaic Solar-Energy Conversion*, IEEE Transactions on Electron Devices **27**, 745 (1980).

[6] W. Ruppel and P. Würfel, *Upper Limit for the Conversion of Solar Energy*, IEEE Transactions on Electron Devices **27**, 877 (1980).

[7] T. Markvart, *The thermodynamics of optical tendue*, Journal of Optics A **10**, 015008 (2008).

[8] M. Green, *Thid Generation Photovoltaics: Ultra-high Conversion Efficiency at Low Cost*, Progress in Photovoltaics: Research and Applications **9**, 123 (2001).

[9] M. Yamaguchi, *IIIV compound multi-junction solar cells: present and future*, Solar Energy Materials & Solar Cells **75**, 261 (2003).

[10] M. Hanna, Z. Lu, and A. Nozik, *Hot carrier solar cells*, AIP Conference Proceedings **404**, 309 (1997).

[11] A. Nozik, *Quantum dots solar cells*, Physica E **14**, 115 (2002).

[12] M. Kelzenberg, S. Boettcher, J. Petykiewicz, D. Turner-Evans, M. Putnam, E. Warren, J. Spurgeon, R. Briggs, N. Lewis, and H. Atwater, *Enhanced absorption and carrier collection in Si wire arrays for photovoltaic applications*, Nature Materials **9**, 239 (2010).

[13] V. Ferry, M. Verschuuren, H. Li, E. Verhagen, R. Walters, R. Schropp, H. Atwater, and A. Polman, *Light trapping in ultrathin plasmonic solar cells*, Optics Express **18**, 128370 (2010).

[14] D. Staebler and C. Wronski, *Reversible conductivity changes in discharge-produced amorphous Si*, Applied Physics Letters **31**, 292 (1977).

[15] E. Yabolovitch, *Statistical ray optics*, Journal of Optical Society of America **72**, 899 (1982).

[16] E. Yabolovitch, *Intensity Enhancement in Textured Optical Sheets for Solar Cells*, IEEE Transactions on Electron Devices **29**, 300 (1982).

[17] Z. Yu, A. Raman, and S. Fan, *Fundamental limit of light trapping in grating sctructures*, Optics Express **18**, 366 (2010).

[18] Z. Yu, A. Raman, and S. Fan, *Fundamental limit of nanophotonic light trapping in solar cells*, Proceedings of the National Academy of Sciences **107**, 17491 (2010).

[19] P. Saeta, V. Ferry, D. Pacifici, J. Munday, and H. Atwater, *How much can guided modes enhance absorption in thin film solar cells?*, Optics Express **17**, 20975 (2009).

[20] H. Deckman, C. Roxlo, and E. Yablonovitch, *Maximum statistical increase of optical absorption in textured semiconductor films*, Optics Letters **8**, 491 (1983).

[21] H. Atwater and A. Polman, *Plasmonics for improved photovoltaic devices*, Nature Materials **9**, 205 (2010).

[22] V. Ferry, M. Verschuuren, H. Li, R. Schropp, H. Atwater, and A. Polman, *Improved red-response in thin film a-Si:H solar cells with soft-imprinted plasmonic back reflectors*, Applied Physics Letters **95**, 183503 (2009).

[23] V. Ferry, M. Verschuuren, H. Li, E. Verhagen, R. Walters, R. Schropp, H. Atwater, and A. Polman, *Light trapping in thin film plasmonic solar cells*, Proc. 25th EU-PVSEC Conference, Valencia (2010).

[24] K. Catchpole and A. Polman, *Design principle for particle plasmon enhanced solar cells*, Applied Physics Letters **93**, 191113 (2008).

[25] P. Spinelli, M. Hebbink, R. de Waele, L. Black, F. Lenzmann, and A. Polman, *Optical Impedance Matching Using Coupled Plasmonic Nanoparticle Arrays*, Nano Letters **11**, 1760 (2011).

[26] L. Kelly, E. Coronado, L. Zhao, and G. Schatz, *The Optical Properties of Metal Nanoparticles: The Influence of Size,*

Shape, and Dielectric Environment, Journal of Physical Chemistry B **107**, 668 (2003).

[27] P. Spinelli, C. van Lare, E. Verhagen, and A. Polman, *Controlling Fano lineshapes in plasmon-mediated light coupling into a substrate*, Optics Express **19**, 303 (2011).

[28] F. J. Beck, E. Verhagen, S. Mokkapati, A. Polman, and K. R. Catchpole, *Resonant SPP modes supported by discrete metal nanoparticles on high-index substrates*, Op **19**, 146 (2011).

[29] H. Stuart and D. Hall, *Enhanced Dipole-Dipole Interaction between Elementary Radiators Near a Surface*, Physical Review Letters **80**, 5663 (1998).

[30] H. Stuart and D. Hall, *Absorption enhancement in silicon-on-insulator waveguides using metal island films*, Appl **69**, 2327 (1996).

[31] H. Stuart and D. Hall, *Island size effects in nanoparticle-enhanced photodetectors*, Applied Physics Letters **73**, 3815 (1998).

[32] H. Zappe, *Fundamentals of Micro-Optics*, Cambridge University Press, 2010.

[33] M. Neviere, R. Petit, and M. Cadilhac, *About the theory of optical grating coupler-waveguide systems*, Optics Communications **8**, 113 (1973).

[34] D. Taillaert, P. Bienstman, and R. Baets, *Compact efficient broadband grating coupler for silicon-on-insulator waveguides*, Optics Letters **29**, 2749 (2004).

[35] B. Auguié and W. Barnes, *Collective Resonances in Gold Nanoparticle Arrays*, Physical Review Letters **101**, 143902 (2008).

[36] G. Vecchi, V. Giannini, and J. Gómez Rivas, *Surface modes in plasmonic crystals induced by diffractive coupling of nanoantennas*, Physical Review B **80**, 201401 (2009).

[37] V. Giannini, G. Vecchi, and J. Gómez Rivas, *Lighting Up Multipolar Surface Plasmon Polaritons by Collective Resonances in Arrays of Nanoantennas*, Physical Review Letters **105**, 266801 (2010).

[38] S. Tikhodeev, N. Gippius, A. Christ, T. Zentgraf, J. Kuhl, and H. Giessen, *Waveguide-plasmon polaritons in photonic crystal slabs with metal nanowires*, physica status solidi (c) **2**, 795 (2005).

[39] M. Verschuuren, *Substrate conformal imprint lithography for nanophotonics*, PhD thesis, Utrecht University, 2010.

[40] M. van Lare, *Plasmonic enhancement of thin film aSi:H solar cells*, Master's thesis, University University, 2010.

[41] A. Polman, *Erbium as a probe of everything?*, Physica B **300**, 78 (2001).

[42] A. Snyder and W. Young, *Modes of optical waveguides*, Journal of Optical Society of America **68**, 297 (1978).

[43] A. Snyder and J. Love, *Optical Waveguide Theory*, Chapman & Hall, 1983.

[44] E. Verhagen, *Subwavelength light confinement with surface plasmon polaritons*, PhD thesis, Utrecht University, 2009.

[45] J. Nelder and R. Mead, *A simplex method for function minimization*, The computer journal **7**, 308 (1965).

[46] *UNL tabulated data for Silicon (from ellipsometry)*.

[47] *Thermal Oxide parametrized for SiO$_2$ (Used by Jenn Dionne)*.

[48] *Lumerical, FDTD Solutions 7 (www.lumerical.com)*.

[49] E. D. Palik, *Handbook for Optical Constants for solids*, Academic, 1985.

[50] *http://docs.lumerical.com/en/fdtd/user_guide_absorption_1.html*.

[51] C. Bohren and D. Huffman, *Absorption and Scattering of Light by Small Particles*, Wiley, 2008.

[52] *Silicon Monoxide - Properties and evaporation techniques, Blevis E.H. and Mathis, R.D.*

[53] *Silicon monoxide evaporation with the multi-baffled box source, Olson, E. and Mathis, R.D.*

[54] G. Hsueh, C. Raeves, S. DenBaars, and W. Weinberg, *Power spectral density analysis of strain-induced InP islands on GaInP/GaAs(100)*, Surface Science **366**, 129 (1996).

[55] T. Itoh and N. Yamauchi, *Surface morphology characterization of pentacene thin film and its substrate with underlayers by power spectral density using fast Fourier transform algorithms*, Applied Surface Science **253**, 6196 (2007).

[56] R. Gavrila, A. Dinescu, and M. D., *A Power Spectral Density Study of Thin Films Morphology Based on AFM Profiling*, Romanian Journal of Information Science and Technology **10**, 291 (2007).

[57] P. Johnson and R. Christy, *Optical Constants of the Noble Metals*, Physical Review B **6**, 4370 (1972).

[58] A. Polman, *Erbium implanted thin film photonic materials*, Journal of Applied Physics **82**, 1 (1997).

[59] G. Franzo, S. Coffa, F. Priolo, and C. Spinella, *Mechanism and performance of forward and reverse bias electroluminescence at 1.54 μm from Er-doped diodes*, Journal of Applied Physics **81**, 2784 (1997).

[60] F. Priolo, G. Franzo, D. Pacifici, V. Vinciguerra, F. Iacona, and A. Irrera, *Role of the energy transfer in the optical properties of undoped and Er-doped interacting Si nanocrystals*, Journal of Applied Physics **89**, 264 (2001).

[61] F. Priolo, G. Franzo, S. Coffa, A. Polman, S. Libertino, R. Barklie, and D. Carey, *The erbium-impurity interaction and its effects on the 1.54 μm luminescence of Er^{3+} in crystalline silicon*, Journal of Applied Physics **78**, 3874 (1995).

[62] E. Snoeks, A. Lagendijk, and A. Polman, *Measuring and Modifying the Spontaneous Emission Rate of Erbium near an Interface*, Physical Review Letters **74**, 2459 (1995).

[63] E. Desurvire, *Erbium-Doped Fiber Amplifiers, Principles and Applications*, Wiley, 1994.

[64] *SRIM (http://www.srim.org/)*.

[65] G. Davies, *The optical properties of luminescence centres in silicon*, Physics Reports **176**, 83 (1989).

[66] P. Catrysse and S. Fan, *Nanopatterned Metallic Films for Use As Transparent Conductive Electrodes in Optoelectronic Devices*, Nano Letters **10**, 2944 (2010).

[67] P. Kuang, J. Park, W. Leung, R. Mahadevapuram, K. Nalwa, T. Kim, S. Chaudhary, K. Ho, and K. Constant, *A New Architecture for Transparent Electrodes: Relieving the Trade-Off Between Electrical Conductivity and Optical Transmittance*, Advanced Materials **XX**, 1 (2011).

[68] M. Kang, M. Kim, J. Kim, and L. Guo, *Organic Solar Cells Using Nanoimprinted Transparent Metal Electrodes*, Advanced Materials **40**, 4408 (2008).

[69] K. Tvingstedt and O. Inganäs, *Electrode Grids for ITO-free Organic Photovoltaic Devices*, Advanced Materials **19**, 2891 (2007).

[70] J. Lee, S. Connor, Y. Cui, and P. Peumans, *Solution-Processed Metal Nanowire Mesh Transparent Electrodes*, Nano Letters **8**, 689 (2008).

[71] S. De, T. Higgins, P. Lyons, E. Doherty, P. Nirmalraj, W. Blau, J. Boland, and J. Coleman, *Solver Nanowire Networks as Flexible, Transparent, Conducting Films: Extremely High DC to Optical Conductivity Ratios*, ACSNano **3**, 1767 (2009).

[72] M. Kang and L. Guo, *Nanoimprinted Semitransparent Metal Electrodes and Their Applications in Organic Light-Emitting Diodes*, Advanced Materials **19**, 1391 (2007).

[73] R.E.I. Schropp, *Nanophotonics research group, Debye institute for Nanomaterials Science, Utrecht University*.

[74] C. Lide, *CRC Handbook of Chemistry and Physics*, CRC Press, 2009.

Acknowledgements